Dynamic changes of optical and chemical properties of tar ball aerosols by atmospheric photochemical aging

Chunlin Li,[†] Quanfu He,[†] Julian Schade,[|] Johannes Passig,[|,‖] Ralf Zimmermann,[|,‖] Daphne Meidan,[†] Alexander Laskin,[§] and Yinon Rudich[†,*]

[†]Department of Earth and Planetary Sciences, Weizmann Institute of Science, Rehovot 76100, Israel

[|]Joint Mass Spectrometry Centre, University of Rostock, Dr.-Lorenz-Weg 2, 18059 Rostock, Germany

[‖]Joint Mass Spectrometry Centre, Cooperation Group 'Comprehensive Molecular Analytics' (CMA), Helmholtz Zentrum München, Ingolstädter Landstrasse 1, 85764 Neuherberg, Germany

[§]Department of Chemistry, Purdue University, West Lafayette, Indiana 47907, United States

Correspondence to: Yinon Rudich (yinon.rudich@weizmann.ac.il)

Abstract. Following wood pyrolysis, tar ball aerosols were laboratory generated from wood tar separated into polar and nonpolar phases. Chemical information of fresh tar balls was obtained from a high-resolution time-of-flight aerosol mass spectrometer (HR-ToF-AMS) and single-particle laser desorption/resonance enhanced multiphoton ionization mass spectrometry (SP-LD-REMPI-MS). Their continuous refractive index (RI) between 365 and 425 nm was retrieved using a broadband cavity enhanced spectroscopy (BBCES). Dynamic changes of the optical and chemical properties for the nonpolar tar ball aerosols in NOx-dependent photochemical process were investigated in an oxidation flow reactor (OFR). Distinct differences in the chemical composition of the fresh polar and nonpolar tar aerosols were identified. Nonpolar tar aerosols contain predominantly high-molecular weight unsubstituted and alkyl-substituted polycylic aromatic hydrocarbons (PAHs), while polar tar aerosols consist of a high number of oxidized aromatic substances (e.g., methoxy-phenols, benzenediol) with higher O:C ratio and carbon oxidation state. Fresh tar balls have light absorption characteristics similar to atmospheric brown carbon (BrC) aerosol with higher absorption efficiency towards the UV wavelengths. The average retrieved RI is 1.661+0.020i and 1.635+0.003i for the nonpolar and polar tar aerosols, respectively, with absorption Ångström exponent (AAE) between 5.7 and 7.8 in the detected wavelength range. The RI fits a volume mixing rule for internally mixed nonpolar/polar tar balls. The RI of the tar ball aerosols decreased with increasing wavelength under photochemical oxidation. Photolysis by UV light (254 nm), without strong oxidants in the system, slightly decreased the RI and increased the oxidation state of the tar balls. Oxidation under varying OH exposure levels and in the absence of NOx diminished the absorption (bleaching), and increased the O:C ratio of the tar balls. The photobleaching via OH radical initiated oxidation is mainly attributed to decomposition of chromophoric aromatics, nitrogen-containing organics, and high-molecular weight components in the aged particles. Photolysis of nitrous oxide (N_2O) was used to simulate NOx-dependent photochemical aging of tar balls in the OFR. Under high NOx condition with similar OH exposure, photochemical aging lead to the formation of organic-nitrates, increased both oxidation degree and light absorption for the aged tar ball aerosols. These observations suggest that secondary organic nitrate formation counteracts the bleaching by OH radical photooxidation to eventually regain some absorption of the aged tar balls aerosols. The atmospheric implication and climate effects from tar balls upon various oxidation processes are briefly discussed.

1 Introduction

Organic aerosol (OA), which represent a ubiquitous and dominant burden of the tropospheric particulate pollutants, play important roles in atmospheric chemistry and balance of regional and global radiation (Jimenez et al., 2009; Kanakidou et al., 2005; Seinfeld and Pandis, 2016; Shrivastava et al., 2017). An indirect climate influence of OA relies on their interaction with water thus acting as cloud condensation nuclei (CCN) that may alter the hydrological cycle (cloud formation and perception) and modify Earth's albedo (Forster and Taylor, 2006; IPCC, 2013; Seinfeld and Pandis, 2016). The direct climate effect of OA is through extinction of incoming solar radiation and outgoing longwave radiation. Of particular importance is the warming effect due to light-absorbing carbonaceous aerosol commonly termed as brown carbon (BrC) (Andreae and Gelencsér, 2006). BrC is an important yet poorly understood OA component due to its complex physical properties, undefined chemical composition, and also its dynamic evolution under atmospheric processes (Adler et al., 2010; Moise et al., 2015; Laskin et al. 2015). It has been estimated that BrC accounts for 10-40% of the total light absorption in the atmosphere and when deposited on snow pack (Bahadur et al., 2012; Park et al., 2010), and contributes to global forcing of 0.10-0.25 W m^{-2}, with even higher values on regional scales (Feng et al., 2013).

The origin of BrC can be either primary (i.e., directly emitted) or secondary (i.e., generated by reactions of aromatic or carbonyl compounds in clouds or particles) (Laskin et al., 2015). On a global scale, biomass burning releases over two-thirds of primary BrC and also contributes substantially to overall secondary OA formation (Jacobson, 2014; Jo et al., 2016). Better understanding of the optical properties of biomass burning BrC aerosols is crucial for constraining its atmospheric and climatic implications and Earth's energy balance. Unlike black carbon that absorbs light strongly throughout the entire UV-visible range, different chromophores that may also be coupled via charge transfer complexes enable BrC absorption in a much more pronounced and complicated wavelength-dependence manner (Phillips and Smith, 2004; Reid et al., 2005; Lin et al., 2016, 2017).

Tar balls are a specific type of particles produced from wood combustion (especially from biomass smoldering burning) which are abundant in the troposphere (Pósfai et al., 2004; Hand et al., 2005; Chen et al., 2017). Tar ball particles have been collected and identified in many biomass burning plumes (Pósfai et al., 2004; Fu et al., 2012; Li et al., 2017). Microanalysis has found that tar balls are homogeneous spherical carbonaceous particles with sizes ranging from tens to hundreds of nanometers. These particles contribute a considerable fraction of the biomass burning BrC (Pósfai et al., 2004; Hand et al., 2005; Li et al., 2017). The estimated burden of tar balls on regional and global climatic forcing has been emphasized (Chung et al., 2012; Jacobson, 2012, 2014).

Tar balls from different burning conditions and bio-fuels coexist with many other types of particles (e.g., inorganic salts, soot, and other carbonaceous aerosols in form of internal or external mixing), and these smoke particles undergo rapid atmospheric processing once they are released from the fire (Pósfai et al., 2004; Hand et al., 2005; Li et al., 2015, 2017). However, *in situ* determination of the optical properties of these particles during their lifetimes in the air has seldom been reported due to inherent difficulty in selective tar balls sampling out of complex particle ensembles typical of field burning emissions.

The complex refractive index (*RI=n+ki, n* and *k* are real and imaginary parts, corresponding to scattering and absorption, respectively) is an intrinsic optical property of aerosols. Quantifying the RI of OA is highly needed for evaluating the related radiative forcing influence (Moise et al., 2015). Recently, several studies have investigated the optical properties of tar ball particles (Chakrabarty et al., 2010; Hoffer et al., 2016; Sedlacek et al., 2018). The optical measurements reported for tar balls or other biomass burning BrC, were discrete over several wavelengths that were constrained by instruments measuring particle light coefficients, or indirectly inferred from calculations based on their electron energy-loss spectra or from UV-Vis absorption of solutions containing dissolved tar balls (Alexander et al., 2008). Hand et al. (2005) measured light scattering coefficients of tar balls-dominated fire plumes using a nephelometer, and reconstructed the scattering coefficients with simplified organic carbon (OC) and elemental carbon (EC) data to get an average RI of 1.56+0.02i for tar balls at λ = 632 nm. Chakrabarty et al. (2010) measured the RI of tar ball particles from smoldering biomass combustion at 405, 532, and 780 nm, they observed a clear wavelength-, biofuel-, and even burning condition-dependent RI. The light absorption by tar balls was similar to humic-like substance (HULIS) with an imaginary part (0.002~0.015) that increased exponentially towards the near UV wavelengths. Recently, Hoffer et al. (2016) generated tar ball particles from flameless wood pyrolysis in the laboratory. They reported a higher RI value of 1.84+0.20i at 550 nm, which fell closer to RI of soot than to that of HULIS. Large discrepancies reside in these results and discrete RI values make it difficult to decipher the complicated wavelength-dependence character of tar balls optical properties, which finally constrains the assessment of its radiative forcing effect.

Freshly emitted smoke BrC contain chromophores with diverse chemical structures, polarity, and volatility (Lin et al., 2016, 2017). After emission into the atmosphere, smoke particles undergo dynamic changes as a result of dilution, precipitation, and chemical processing on scales of seconds to days, which eventually affect the physiochemical properties of BrC particles during their lifetimes in the atmosphere (Reid et al., 2005; Li et al., 2015; Laskin et al., 2015). Sumlin et al. (2017) simulated atmospheric photooxidation of biomass burning BrC, and reported that photooxidation diminishes their light absorption. Zhong and Jang (2014) investigated the

influence of humidity and NOx presence in photochemical aging of biomass burning BrC. They found that sunlight faded the color of BrC, and humidity facilitated the decay of light absorption by BrC, while presence of NOx delayed the fading. Overall, they concluded that light absorption by BrC is governed by chromophores formation and bleaching by sunlight in the atmosphere. Therefore, evaluating the climatic impacts of tar ball particles requires more extensive investigation of its optical properties, and understanding of the dynamic transformations of the optical properties during atmospheric aging.

In this study, we generated proxies for tar ball particles by flameless wood pyrolysis (Tóth et al., 2014; Hoffer et al., 2016). This method allows consistent and continuous generation of tar ball proxy aerosols for studying their properties and processes. The RI of the tar aerosols as a function of wavelength in the ultraviolet-short visible region (365~425nm, 0.5 nm resolution) was determined using a broadband cavity enhanced spectrometer (BBCES). A high resolution time of flight aerosol mass spectrometer (HR-ToF-AMS) and a single-particle mass spectrometer applying laser desorption/resonantly enhanced multiphoton ionization (SP-LD-REMPI-MS) were used for probing the chemical profile of tar ball aerosols under NOx-dependent multiple-day photochemical oxidation. Specifically, the dynamic changes of their optical properties in correlation with their chemical composition were investigated. The atmospheric implications and climate forcing due to atmospheric aging of tar aerosols and evolution of their optical properties were also explored.

2 Experiment

2.1 Tar ball particle generation

Following the formation mechanism in biomass burning process, polydisperse tar ball particles were generated from droplets of wood tar in the laboratory (Tóth et al., 2014; Hoffer et al., 2016). In this study, a similar procedure was applied for producing tar ball aerosols. In brief, commercial wood pellets (Hallingdal Trepellets, water content of 6.55 wt.%, size of 2~3 cm in length, 0.2-0.3 cm in diameter) were smashed, heated and dry-distillated in absence of air (25^{o}C min^{-1} increase to 530 ^{o}C from room temperature, and held for 20 min at 530 ^{o}C) to produce liquid tar-water emulsions (~25 mL per hundred grams of used wood pellets). The emulsions were filtrated using 0.45 μm pore size filters (PTFE membrane, diameter 47 mm, Pall Corp.) to remove particulate matter or solid precipitation. After overnight static stabilization, the wood tar solution was phase-separated into water soluble and non-soluble oily phases at an initial 3:1 volume ratio. Herein, we will term these two fractions as 'polar' and 'nonpolar' phases, respectively. The phase-separated solution was further concentrated using a heating plate at 300 ^{o}C with N_2 purge flow to prevent oxidation. A final 1:1 volume ratio of polar to nonpolar phase was obtained; then the concentrated

126 solutions were sealed and stored in the dark under 2 °C for following experiments. With respect to their potential
127 reactivity and instability, the distillation products were used within a few days.

128 For particle optical measurement, tar balls were produced from aerosolization of above predefined wood tar
129 diluted in methanol (Gradient grade for HPLC, purity≥99.9 wt.%, Merck) using a constant output atomizer (Model
130 3076, TSI) with high-purity N_2 as a carrier gas. As the actual fractions of the polar and nonpolar compounds
131 contributing to the mass of ambient tar ball or biomass burning organic aerosol (BBOA) can vary with biofuel
132 sources, burning condition, atmospheric process, and also method/efficiency to classify the polar and nonpolar
133 materials from the sample (Sengupta., et al., 2018; Lin et al., 2017, 2018; Chen and Bond, et al., 2010; Rajput et
134 al., 2008), tar ball aerosols in this study were generated from polar, nonpolar, and mixtures of two phase tar
135 solutions at volume mixing ratio of 2:1, 1:1, and 1:2, respectively. Activated charcoal denuders and quartz heating
136 tube (150 °C, residence time ~0.7s for particles at a nitrogen flow of 1.0 LPM) were used after the atomizer to
137 outgas the methanol from the gaseous and particulate phases. Mesh filters (TSI) downstream were used to filter
138 out some ultrafine (less than 100 nm) particles.

139 **2.2 NOx-dependent OH oxidation of tar ball aerosols**

140 Heterogeneous oxidation of tar ball aerosols was simulated using an oxidation flow Reactor (OFR), shown
141 schematically in Fig. 1. The OFR has been characterized (Kang et al., 2007; Peng et al., 2015, 2016) and the
142 operational procedures have been described previously (He et al. 2018). Briefly, the OFR consists of a horizontal
143 13.3 L aluminum cylindrical chamber (46 cm long × 22 cm ID) operating in continuous flow mode. The chamber
144 is equipped with two power controllable ozone-free mercury-lamps with peak emission at λ= 254 nm (82-934-08,
145 BHK Inc., CA, USA). The two UV lamps are surrounded by Pyrex sheath tubes that are continuously purged with
146 N_2 to cool the lamps and remove outgassing compounds. OH radicals in the OFR are produced through photolysis
147 of externally introduced O_3 under 254 nm illumination and the further reaction of singlet oxygen (O^1D) with water
148 vapor:

149 $$O_3 + h\nu(254nm) \rightarrow O^1D + O_2 \quad \text{R1}$$

150 $$O^1D + H_2O \rightarrow 2OH \quad \text{R2}$$

151 External O_3 was produced by irradiation of 0.2 LPM high purity O_2 using a mercury lamp (λ=185nm, 78-2046-
152 07, BHK Inc., CA). The O_3 concentration downstream of the OFR was measured by an O_3 monitor (2B
153 Technology). A Nafion membrane humidifier (Perma Pure LIC, NJ) was used to supply water vapor to the OFR.
154 Tar ball aerosols carried by 1.0 LPM N_2 flow from the atomizer were introduced into OFR. The initial aerosol

concentrations in the OFR were mediated by controlling the concentration of the wood tar solution to be atomized until the number of 350 nm particles was above 100 cm^{-3}, as shown in Fig. S1 of tar ball aerosols size distribution (SI, supporting information). Finally, a total flow of 5.5 LPM with 36~38% RH, initial 27~28 ppm O_3, and 200~250 μg m^{-3} tar ball particles (assuming material density of 1.0 g cm^{-3}) was maintained, with a corresponding plug flow residence time (RT) of 144s for aerosols in the OFR.

The extent of simulated daytime oxidation by OH exposure was varied by changing the UV light intensity. Here, OH exposures in the OFR were inferred by measuring the decay of added SO_2 (monitored by Thermo SO_2 analyzer, model 43i) due to reaction with OH radicals at specific UV lamp intensity. A low concentration (~60ppb) of SO_2 was used to minimize its influence on the OH radical reactivity. Typical total OH exposures ranged from $(8.7\pm2.3)\times10^{10}$ to $(8.6\pm1.7)\times10^{11}$ molec cm^{-3} s or 0.5~7 equivalent daytime atmospheric oxidation days (EAD) were maintained, taking typical ambient average OH concentration as 1.5×10^{6} molec cm^{-3} (Kang et al., 2007; Peng et al., 2015, 2016).

In addition to reactions with oxidants, organic aerosols may change their chemical and physical properties by photolysis (Epstein et al., 2014; Lee et al., 2014; Wong et al., 2014). Therefore, the influence of light irradiation during tar ball photochemical aging was assessed at the short exposure time in the OFR. Here, tar balls aging was repeated at the same conditions (e.g., RT, RH, N_2/O_2 flow, tar balls concentration, UV lamp power) without O_3 supply in the OFR. The 254 nm photon flux at specific to maximal UV lamp power was calculated by fitting the OH exposure estimated from SO_2 decay and by the Aerodyne OFR Exposure Estimator (v3.1, https://sites.google.com/site/pamwiki/hardware/estimation-equations).

Under polluted conditions, nitrogen oxides (NOx) are often involved in the atmospheric transformations of organic aerosol and alter their physiochemical properties (Rollins et al., 2012; Ng et al., 2007; Lin et al., 2015). Therefore, NO_x influence on tar ball aerosol aging was also investigated. Due to rapid conversion of NOx ($NO+NO_2$) into nitric acid (HNO_3) under high O_3 and OH concentrations, simple addition of NOx into OFR cannot sustain NOx levels that compete with HO_2 radicals in the reaction with organic proxy (ROO). NOx generated via N_2O reaction with O^1D has been modeled and tested to suit the characterization of NOx-dependent SOA formation pathways using OFR (Peng et al. 2017; Lambe et al., 2017). In this study, N_2O (99.999%) addition of 0.5 vol.% and 2.0 vol.% were used during tar ball aerosol photochemical oxidation in the OFR, and equivalent OH exposure of about 4.0 EAD was maintained. NO_x (NO and NO_2) concentrations downstream of the OFR was measured using a NO/NO_2 analyzer (Ecotech, Serinus 40 NOx). Experimental parameters including initial O_3 and N_2O concentrations, NOx, moisture ratio, maintained OH exposures and the corresponding photon flux at 254 nm are

185 presented in Table 1.

186 **2.3 Online optical and chemical characterization**

187 Prior to the optical and chemical measurements, excess ozone and NOx were removed from the sample air stream
188 following the OFR using two diffusion denuders packed with Carulite (Carus Corporation, Peru, IL) and one
189 activated charcoal tube. The stream flow was further dehydrated with two silica gel diffusion dryers. Afterward,
190 the tar ball aerosols were characterized by a combination of on-line chemical and optical instruments.

191 Bulk chemical fragments and organic elemental ratios of tar ball aerosols were monitored in real time by the
192 HR-ToF-AMS (Aerodyne Research Inc., Billerica, MA, USA) in alternating high sensitivity V and high-resolution
193 W modes. The working principles of the AMS have been described in details elsewhere (DeCarlo et al., 2006). In
194 short, aerosol particles are separated from the gas phase through an aerodynamic lens system and then transferred
195 into the vacuum system, where they are impacted onto a vaporizer at about 600 ^{o}C, thus vaporizing the particles.
196 The analyte vapors are ionized with 70 eV electron impact ionization (EI). A time-of-flight mass spectrometer is
197 used for high-resolution analysis of the ions. SQUIRREL v1.16 and PIKA v1.57 codes
198 (http://cires.colorado.edu/jimenez-group/ToFAMSResources/ToFSoftware/) were used to process the collected
199 AMS data. Four ion groups were classified as $C_xH_y^+$, $C_xH_yO^+$, $C_xH_yO_z^+$ (z>1), and $C_xH_yO_iN_p^+$(i≧0, p≧1) based
200 on fragment features. The ions O^+, OH^+, and H_2O^+ were included in the $C_xH_yO_z^+$ group, as concentrations of these
201 species were calculated from the organic CO_2^+ ion abundance using the method in Aiken et al (2008). The ambient
202 improved (AI) atomic ratios of oxygen to carbon (O:C), hydrogen to carbon (H:C), nitrogen to carbon (N:C), and
203 organic mass to organic carbon (OM/OC) were generated from the measured ion fragments.

204 Particle-bound organic molecules were measured using a custom single-particle time-of-flight mass
205 spectrometer. This instrument features laser desorption and resonantly enhanced multiphoton ionization (SP-LD-
206 REMPI-ToF-MS), allowing for the detection of aromatic substances on individual particles. Detailed description
207 and application of the instrument in LD-REMPI ionization mode is given by Bente et al. (2008) and Passig et al.
208 (2017). Briefly, aerodynamically accelerated particles are individually sized using laser velocimetry, and heated
209 by a pulsed CO_2 infrared laser (10.6 μm) to desorb organic molecules. Aromatic substances in the gas plume are
210 selectively ionized via REMPI by a KrF-excimer laser pulse (248 nm) and detected in the positive MS flight tube.
211 The REMPI-MS technique is very sensitive and selective for aromatic substances (Boesl et al., 1978; Grotemeyer
212 et al., 1986; Rettner and Brophy, 1981) and suitable for studies on pyrolysis and (wood) combustion processes
213 (Heger et al., 1999; Czech et al., 2017). For the tar ball aerosols it provides complementary information to the

HR-ToF-AMS spectra. A custom software on LabView basis records and calculates the aerodynamic size and individual mass spectra of the particles.

For optical measurements, tar ball aerosols were size-selected using an Aerosol Aerodynamic Classifier (AAC, Cambustion, UK). AAC has significant advantages over the commonly used Differential Mobility Analyzer (DMA) classifier. The AAC classifies particles based on the aerodynamic size without charging and hence it avoids the contribution of multiply charged particles, thus generating real monodisperse size-selected particles distribution, reducing the errors associated with multiply charged large particles. In addition, the AAC has higher particle transmission efficiency at the relevant size range (Tavakoli and Olfert, 2013, 2014). Aerodynamic size-classified particles after the AAC were further scanned by a scanning mobility particle sizer (SMPS, classifier Model 3080, DMA Model 3081, CPC model 3775, TSI) to derive their mobility size distribution. The effective density of tar balls can be estimated from Equation 1 with assumptions of homogeneous composition and particle shape factor of 1.0, which was verified later in this study:

$$\rho_{eff} = \frac{D_{aero}}{D_m}\rho_0 \quad [1]$$

Where ρ_{eff} is an effective density, D_{aero} and D_m are aerodynamic and mobility diameters, respectively. ρ_o is unit density of 1.0 g cm^{-3}.

Based on the derived effective density, size-specific tar ball aerosols covering mobility diameters between 175 to 350 nm with an interval of 25 nm were size-selected via AAC, and monodisperse tar balls were introduced into a dual-channel broad-band cavity enhanced spectrometer (BBCES) for light extinction (α_{ext}) measurements in the wavelength of 360~395 nm and 385~435 nm (at resolution 0.5 nm). A detailed description of the instrument can be found elsewhere (Washenfelder et al., 2013; Flores et al., 2014a, b). With the combination of a condensation particle counter (CPC, Model 3575, TSI) to measure particle concentration (N) in series, size-specific particle extinction cross section (σ_{ext}) can be calculated by Equation (2):

$$\sigma_{ext}(\lambda, Dp, RI) = \frac{\alpha_{ext}(\lambda, D_p, RI)}{N(D_p)} \quad [2]$$

Where λ is the wavelength of incidence light, D_p is the particle mobility diameter.

Using the Mie-Lorenz scattering theory, the wavelength-dependent complex refractive index of spherical homogeneous particles was derived (Pettersson et al. 2004; Abo Riziq et al. 2007). The retrieval algorithm was limited to search for n≧1 and k≧0 as their physical boundaries. Thereafter, spectral dependent extinction, scattering, and absorption cross sections (σ_{ext}, σ_{sca}, and σ_{abs}) were calculated from the complex RI at specific particle size. Using these parameters, the single scattering albedo, indicating the scattering fraction of light

extinction (SSA = $\sigma_{sca}/\sigma_{ext}$), was calculated.

The absorption and extinction Ångström exponents ($Å_{abs}$ and $Å_{ext}$) describe the spectral dependence of aerosol light properties, and are widely used in climate modeling (Russell et al., 2010). It is customary to extrapolate the optical spectral absorption and extinction fitting to the range of wavelengths using a power law $\propto\lambda^{-Åabs}$ and $\propto\lambda^{-Åext}$, respectively. In this work, we determined $Å_{ext}$ and $Å_{abs}$ with a linear regression of $\ln(\sigma_{ext})$ and $\ln(\sigma_{abs})$ against $\ln(\lambda)$ over the range of 365 to 425 nm:

$$Å_{ext} = -\frac{\ln(\sigma_{ext})}{\ln(\lambda)} \qquad Å_{abs} = -\frac{\ln(\sigma_{abs})}{\ln(\lambda)} \quad [3]$$

Here $Å_{ext}$, $Å_{abs}$, and SSA were calculated for tar ball aerosols with a median diameter of 150 nm.

2.4 Offline optical characterization

In addition to the *in-situ* measurements, tar ball particles were also collected quantitatively onto Teflon filters (47 mm diameter, 0.45 μm porosity, Pall Corp.) at sampling flow rate of 2 LPM and then extracted using methanol (HPLC grade, purity≥99.9%, Merck) for offline UV-Vis absorption measurement (Cary 60 UV-VIS spectroscopy, Agilent). Methanol extraction of organic compounds has been commonly performed in various studies (Hoffer et al., 2006; Laskin et al., 2009; Yee et al., 2013; Finewax et al., 2018; Xie et al., 2017). Here we verified the completeness of the extraction by extracting each filter twice with methanol. Moreover, vortex shaking (Vortex Genie-2, Scientific Industries) rather than sonication was applied to avoid chemical degradation of the extracts upon ultrasonic irradiation (Miljevic et al., 2014; Mutzel et al., 2013). The methanol extractable BrC mass absorption cross section (MAC, $m^2\ g^{-1}$) and refractive imaginary k of the tar balls were estimated based on following relations (Chen and Bond, 2010; Laskin et al., 2015):

$$MAC_{(\lambda)} = \frac{Abs_{(\lambda)} \times \ln(10)}{C \times b} \quad [4]$$

$$k_{(\lambda)} = \frac{\lambda \times \rho \times MAC_{(\lambda)}}{4\pi} \quad [5]$$

$Abs_{(\lambda)}$ is the base-10 absorbance result from UV-VIS spectroscopy (unitless), b is the optical length of the solution (1 cm), C is the extracted organic carbon mass concentration in solvent ($g\ m^{-3}$), which can be determined directly by normalizing the extract concentration and OC mass fraction for tar balls as OC/OM obtained from AMS data, as no other refractory elemental carbon (EC) content was detected in our samples (details see in SI). λ is the incident light wavelength, and ρ is material density ($g\ cm^{-3}$). Here, the derived effective density ρ_{eff} was used. The absorption Ångström exponent based on MAC was also derived as $Å_{abs\text{-}UV\text{-}Vis}$ over the 365-425 nm spectral range.

In addition, particles were impacted at a flow of 2.5 L min^{-1} onto cyclopore track-etched polycarbonate

membrane (47 mm, 0.1μm porosity, Whatman Inc.) to investigate the morphology of tar balls using Scanning Electronic Microscopy (SEM, JEOL JSM-7000F).

2.5 Radiative impacts of tar ball aerosols

To assess the climatic influence of tar ball aerosols, a wavelength-dependent direct shortwave aerosol simple radiative forcing efficiency (SRF, W g^{-1}) was estimated using the clear sky air mass global horizonal solar spectrum (AM1GH), assuming that tar ball aerosols form a uniform, optically thin aerosol layer at the lower troposphere or on ground (Bond and Bergstrom, 2006; Levinson et al., 2010):

$$\frac{dSRF}{d\lambda} = -\frac{1}{4}\frac{dS_{(\lambda)}}{d\lambda}\tau_{atm(\lambda)}^{2}(1-F_c)[2(1-R_{sfc})^{2}\beta_{(\lambda)}MSC_{(\lambda)} - 4R_{sfc}\cdot MAC_{(\lambda)}] \quad [6]$$

Where $dS(\lambda)/d\lambda$ is the solar irradiance (photons s^{-1} cm^{-2}), τ_{atm} is the atmospheric transmission (taking 0.79 for simple calculation), F_c is the cloud fraction (approximately 0.6), R_{sfc} is the surface albedo (approximate 0.19 for urban area ground and 0.8 for snow) (Chen and Bond, 2010), β is the average up-scatter fraction (the fraction of scattered sunlight that is scattered into the upward hemisphere), and $MSC(\lambda)$ is wavelength-dependent mass scattering cross section, respectively. We simply calculated radiative forcing of particles with atmospheric relevant size of 50 to 500 nm, and SRF was estimated and integrated over the measured range of 365~425nm. The actinic flux over 365~425 nm was obtained from the "Quick TUV Calculator", available at http://cprm.acom.ucar.edu/Models/TUV/Interactive_TUV/ using the following parameters: SZA (solar zenith angle) of 0 degree, noon time, June 30, 2000, 300 Dobson overhead ozone column, surface albedo of 0.19 for urban area and 0.8 for snow, and 0 km altitude.

3 Results and discussion

3.1 Chemical composition and optical properties of fresh tar ball aerosols

Negligible fractions of inorganics (e.g., sulfate, nitrate, chloride, and ammonium) in tar balls are obtained from AMS measurement as shown in Fig. S2 (SI), and these results confirm again that tar ball aerosols contain dominated carbonaceous compounds with minor amounts of N, S, and Cl (Pósfai et al., 2004; Hand et al., 2005; Adachi and Buseck, 2011). Thereafter, only organics in tar balls are considered, and the high-resolution bulk organic mass spectra for polar and nonpolar tar ball particles are given in Fig. 2. The mass spectra features and particle effective densities are summarized and compared in Table S1 (SI). Distinct differences in the chemical composition were observed between polar and nonpolar tar ball aerosols. The alkyl fragments ($C_xH_y^+$, e.g., $C_nH_{2n-1}^+$, $C_nH_{2n+1}^+$) dominate the signals for nonpolar particles (accounting for ~56% of total fragments), implying that

the nonpolar tar balls have compositional similarity with common hydrocarbon organic aerosol (HOA). The $C_xH_yO^+$ fragments are the primary ions for the polar tar balls, contributing ~42% of their mass spectrum, suggesting that most of the organic constituents in the polar tar balls are substantially oxygenated. Both spectra exhibit significant intensity at *m/z* 28 (CO^+), *m/z* 29 (CHO^+), and *m/z* 43 ($C_2H_3O^+$), indicating the presence of carbonyl ions. The strong signal at *m/z* 31 (CH_3O^+) results from methoxy species that preferably partition into the polar tar fraction. In addition, the significant signals at *m/z* 50-52 ($C_4H_2^+$, $C_4H_3^+$, $C_4H_4^+$), *m/z* 65 ($C_5H_5^+$), *m/z* 77-78 ($C_6H_5^+$, $C_6H_6^+$), *m/z* 81 ($C_6H_9^+$), and *m/z* 91 ($C_7H_7^+$), which are characteristic of aromatic compounds, indicate that tar balls, especially from the nonpolar phase, contain a considerable amount of aromatic organics or present high aromaticity. Ion peaks at *m/z* 77-78, 81, and 91 are typical for monocyclic aromatics such as alkyl-substituted benzene (for *m/z* 77-78, 91) and heterocyclic aromatics (for *m/z* 81) (Li et al., 2012). While the relative higher signal at *m/z* 128 ($C_{10}H_8^+$) in the nonpolar tar ball mass spectra can be assigned to molecular ion of naphthalene (Herring et al., 2015). Moreover, signals at *m/z* 55 and 57 ($C_3H_3O^+$, $C_3H_5O^+$) are signature fragments of aliphatic and non-acid oxygenated organics that are used to trace cooking emissions (He et al., 2010), and these two fragments were also observed in the tar ball aerosols. Similar to ambient biomass burning emissions, $C_2H_4O_2^+$ (*m/z* 60) and $C_3H_5O_2^+$ (*m/z* 73), two characteristic fragments from levoglucosan and similar cellulose pyrolyzed species (e.g., mannosan, galactosan) were detected in all the tar ball aerosols, and these fragments were more prominent in the polar aerosols due to the solubility of levoglucosan and analogs in water. Weimer et al. (2008) reported the percentage of *m/z* 60 and 73 for the burning of various woods to be 0.6-4.1% and 0.1-2.0%, respectively. The percentage of these two fragments in our tar ball aerosols (0.7-1.6% for *m/z* 60 and 0.5-0.9% for *m/z* 73) are comparable to the literature data, although the fuel and the pyrolysis procedure are different. The *m/z* 137 peak is dominated by fragments of $C_8H_9O_2^+$ and $C_7H_5O_3^+$, and these fragments have been determined in biomass burning emissions and were assigned to lignin-related ions with methoxy-phenolic structures (Li et al., 2012; Li et al., 2014). Phenols and methoxy phenols are prominent compounds, accounting for 41% of the identified organic species, in primary BBOA (Schauer et al., 2001). The signal at *m/z* 137 is much higher in the nonpolar phase tar ball aerosols (1.0% and 0.5% for nonpolar and polar tar balls, respectively), and the fraction of fragment *m/z* 137 is consistent with reference values of 0.3-2.0% (Li et al., 2012). *m/z* 44 (CO_2^+), a marker fragment of carboxylic acids has been parameterized as *f*44 (fraction of mass spectrum signal at *m/z* 44) to present the oxidation degree of organic aerosols (Aiken et al., 2008; Ng et al., 2010). Higher *f*44 values indicate more oxidized OA (OOA), while less oxidized OA is characterized by lower *f*44 (Schauer et al., 2001). Peroxides can also produce CO_2^+ signal via extensive fragmentation in the AMS (Aiken et al., 2008). *f*44 has also been shown

to be linearly correlated with the elemental O:C ratio of OA (Aiken et al., 2008). In this study, $f44$ for the nonpolar and polar tar ball aerosols are 1.9% and 2.4%, and the corresponding O:C ratios are 0.25 and 0.44. The higher O:C and H:C ratios explain the polarity of the polar tar ball aerosols. The simplified average carbon oxidation state ($\overline{OSc}$≈2O:C-H:C) describe the oxidation level of particulate complex organic mixtures (Kroll et al., 2011). The calculated $\overline{OSc}$ for the tar ball aerosols are -1.05~-0.76, which agrees well with reference values of -1.0~-0.7 for primary BBOA (Kroll et al., 2011). These values are in the broad range of -1.7~-1.6 for HOA and -0.5~0 for semivolatile OOA (Aiken et al., 2008). In addition, a small fraction of nitrogen-containing organic compounds (NOC) was detected, with the $C_xH_yO_iN_p^+$ group contributing 1.6~3.6% of the tar ball mass spectra with estimated N:C ratio below 0.01, which agrees with previously reported N:C values of 0.008~0.018 for biomass burning emissions (He et al., 2010). Biomass burning is an important source of NOC in the atmosphere, alkaloid and nitro-aromatic constituents were detected to be abundant constituents of the NOC (Laskin et al., 2009; Lin et al., 2017). Nitroaromatic compounds were also identified in urban fire emissions (Bluvshtein et al., 2017; Lin et al., 2017). Although these compounds constitute a small fraction of the BBOA mass, these chromophoric NOC species accounted for 50~80% of the total visible light absorption by the extractable BrC (Lin et al., 2017).

Fragments larger than 100 amu ($f_{m/z>100}$) contribute a large fraction of the total organic signals for tar ball aerosols, consistent with biomass burning emissions that contain a large fraction of high-molecular weight compounds (Ge et al., 2012; Zhou et al., 2017). $f_{m/z>100}$ is 32% for the nonpolar tar ball aerosols, which is higher than that of the polar particles (15%), demonstrating that the nonpolar tar balls consists of more high-molecular weight organics. The measured effective densities for polar and nonpolar tar balls are 1.33 and 1.24 g cm^{-3}. Chemical characteristics from AMS and densities for internal mixture tar balls follow the volume-linear mixing of polar and nonpolar tar solutions.

A considerable aromatic fraction in the tar ball aerosols was confirmed by the LD-REMPI-MS measurement. Fig. 3 presents the mass spectra of aromatic substances obtained for each one exemplary polar and one nonpolar particle, respectively. Aerodynamic size distributions for the detected tar ball aerosols are given in Fig. S3, and substances identified in the mass spectra are listed in Table S2 (SI). The features in the mass spectra are consistent with the polarity of examined tar ball aerosols and ambient BBOA (Lin et al., 2018). The complex REMPI-spectrum shows rows of intense unsubstituted and partially alkylated PAH peaks in the nonpolar tar balls, including naphthalene, acenaphthylene, phenanthrene, pyrene, and in particular, the softwood combustion marker retene at *m/z* 234 and some possible derivatives (oxidized-retene at *m/z* 250 with one oxygen addition, methyl-retene at *m/z* 248 with one methyl addition) (McDonald et al., 2000; Shen et al., 2012). Retene and some of the

aforementioned PAHs are also observed in the polar tar ball aerosols' mass spectra with lower intensities. In contrast, the polar tar ball REMPI mass spectra shows strong peaks from oxidized aromatics, more specifically, benzenediol and methoxy-phenols (e.g., catechol, guaiacol, acetovanillone, syringaldehyde, conifery aldehyde, etc.). These results are also verified in ambient BBOA, of which the nonpolar BrC consists of primary unsubstituted PAHs, while the polar fraction includes major aromatic acids and phenols (Lin et al., 2018). The REMPI mass spectra corresponds to the large fractions of CHO^+ and CH_3O^+ fragments and high O:C ratios observed for the polar tar aerosols via HR-ToF-AMS, and keep in consistence with the strong signals of typical aromatic fragments observed in the nonpolar tar aerosols in Fig. 2. The dominance of aromatic compounds in tar ball chemical composition agrees well with previous work on BBOA (Schauer et al., 2001; Wei et al., 2015; Bente et al. 2008, 2009; Czech et al. 2017). Biomass burning is a major source of environmental PAHs (alkylated PAHs, oxygenated-PAHs, phenols, nitrogen-substituted PAHs, etc.) in both particulate and gaseous phases, and extensive emissions of PAHs from incomplete combustion pose a great threat to ecosystem and human health due to their carcinogenic toxicity (Li et al., 2017; Shen et al., 2013; Sigsgaard et al., 2015; Shrivastava et al., 2017). Moreover, the primary PAHs can act as precursors that substantially contribute to ambient SOA or BrC aerosol when involved in atmospheric photochemical aging, leading to profound climatic influence (Yee et al., 2013; Yu et al., 2014; Lu et al., 2011; Zhang et al., 2012).

The complex refractive index (RI) of tar ball aerosols was retrieved under the assumption that the particles have similar chemical composition and a spherical shape. The SEM images shown in Fig. S4 (SI) confirm the spherical morphology and homogeneous composition of the tar ball particles generated in this study. Electron energy-loss spectroscopy (EELS) spectra indicates that the tar ball particles contain major C and minor O, which fits the AMS result and previous work (Pósfai et al., 2004; Chakrabarty et al., 2010). Continuous spectral-dependent RI and SSA for tar balls were derived and are presented in Fig. 4, RI results for tar ball aerosol at mixing ratio of 2:1 and 1:2 are presented in Fig. S5 (SI). Although scattering dominates the light extinction, absorption in the UV and in the visible ranges was unambiguously identified for the tar ball aerosols, with characteristic absorption similar to atmospheric BrC and HULIS (Hoffer et al., 2006; Bluvshtein et al., 2017; Lin et al., 2017). The imaginary part, *k*, increases towards the UV range, presenting 0.02~0.03 difference over the measured spectra range. The real part, *n,* for the nonpolar tar balls decreased from 1.673 at 365nm to 1.647 at 425nm, which is almost parallel to the descending *n* for the polar tar balls ranging from 1.651 at 365nm to 1.625 at 425nm. *k* is 0.029~0.013 for the nonpolar tar ball over light wavelength of 365~425nm, while the imaginary part for nonpolar aerosols is 0.007 at 365nm and zero at wavelength longer than 410 nm, indicating that there is no detectable absorption or *k* is lower

than our detection limit. The overwhelming imaginary part for the nonpolar tar aerosol agrees with many reports that nonpolar or less polar organics have higher absorption compared with the polar BrC in BBOA (Lin et al., 2018; Sengupta et al., 2018). The stronger absorption and relative higher scattering abilities, resulting in a lower SSA compared with the polar tar ball aerosols. The SSA increases towards the visible wavelength from 0.86 at 365nm to 0.90 at 425nm for nonpolar tar ball, and the corresponding values are 0.95 to 1.0 for the polar tar balls.

The optical properties of aerosols relate to their chemical composition. Evidently, most of the PAHs identified in the tar ball aerosols with high intensity have strong absorption between 350 and 450nm (Samburova et al., 2016; Lin et al., 2018), as shown in Fig. S6 (SI), which coincide the range of tar ball absorption measured here, implying that PAHs could be a dominate contributor to the absorption of fresh tar balls. Higher imaginary *k* can be explained partly by the larger proportion of PAHs as well as more high-molecular-weight organics present in the nonpolar tar ball particles, as conjugated aromatic rings and phenols contribute to the major chromophores in the wood smoke (Laskin et al., 2015; Lin et al., 2017, 2018). High-molecular weight organics may resemble HULIS that can form charge transfer complexes (Phillips and Smith, 2004), that can absorb light at a longer wavelength range. The result is consistent with the finding that higher molecular weight and aromaticity result in stronger absorption for atmospheric BrC (Dinar et al., 2008). Moreover, the higher NOC content may also contribute to the chromophores in the nonpolar tar aerosols (Lin et al., 2017, 2018).

The average RIs at 375 and 405 nm are 1.671+0.025*i* and 1.659+0.017*i* for nonpolar tar ball aerosols. The corresponding RIs are 1.647+0.005*i* and 1.635+0.04*i* for the polar tar ball aerosols. The imaginary part *k* retrieved from the BBCES data, though low, agrees well with *k* values calculated from UV-Vis absorption of the bulk solution. The MAC for the methanol extracted BrC in tar ball aerosol is shown in Fig. S7 (SI). The absorption may be different for complex materials in the particulate and in the aqueous phases since parameters such as shape factor, mixing state, together with artifacts from the optical instruments detection and data retrieval methods can all affect the final optical results, while solvent-dependent extraction/dissolving efficiency of chromophores or solvent effect (e.g., pH in water solution) may impact the solution absorption coefficient (Huang et al., 2018; Lin et al., 2017). The light absorption coefficient of particulate BrC has been reported to be 0.7~2.0 times that of bulk BrC extracts by Liu et al. (2013).

The absorption Ångström exponent ($Å_{abs}$) is often used to describe the wavelength-dependence of aerosol light absorption with a value of nearly 1 for BC particles and values substantially larger than 1 indicating the contribution from BrC (Reid et al., 2005; Chen and Bond, 2010). In this work, $Å_{abs}$ for the nonpolar and polar tar ball particles ranges from 5.9 to 6.8 between 365 and 425 nm, which is consistent with values of 5.7~7.8 calculated

from the bulk absorption in solution. The nonpolar tar balls have a lower $Å_{abs.}$ The difference in $Å_{abs}$ reflects the different chemical composition of chromophores in the particles, as inferred also from the AMS data. Bluvshtein et al. (2017) reported relative low values of $Å_{ext}$ (2~3) and $Å_{abs}$ (4~6) over 300~650 nm for ambient fire plume, which are likely affected by BC in the smoke aerosol and also due to lower wavelength dependence of aerosol absorption and scattering over the longwave visible range. Overall, the broadband optical results for fresh tar ball aerosols are consistent with limited discrete measurements of atmospheric BBOA as summarized in Table 2. It has also been found that the biomass fuel type, combustion conditions, and atmospheric processing eventually affect the optical properties of BBOA. Lack et al. (2012) modeled core-shell absorption for primary organic matter (POM) and BC from biomass burning. They found that the imaginary part of the RI and BrC MAC of POM at 404 nm were 0.007±0.005 and 0.82±0.43 m^2 g^{-1}, respectively. Charkey et al. (2010) compared the optical properties of tar balls from smoldering combustion of different biomass. Fuel-dependent imaginary RI for tar ball at 405 nm was 0.008~0.015 and $Å_{abs}$ over 405~532 nm was 4.2~6.4, which is in line with the $Å_{abs}$ value of 6~7 reported for BBOA derived HULIS (Hoffer et al., 2006). Sedlacek et al. (2018) observed a weak absorption for wildfire produced tar balls with RI of 1.56 +0.02i. Sumlin et al. (2018) simulated BrC formation under different pyrolysis temperatures. The BrC produced from over 300 ^oC combustion has imaginary part *k* of 0.05~0.09 and real part *n* of 1.59~1.68 at 375 nm, and RI at 405 nm is 1.57+0.03i, corresponded $Å_{abs}$ over 375~405 nm is 6.4~7.4.

Optical mixing rules can be used to estimate or explain the refractive indices of internally mixed substances, and three mixing rules are commonly applied in climate models: molar refraction of absorption (Jacobson, 2002), volume-weighted linear average of the refractive indices (d'Almeida et al., 1991), and the Maxwell-Garnett rule (Chýlek et al., 2000). The “linear mixing rule” and molar refraction mixing rules were tested in this work for mixtures of tar ball particles against the retrieved optical data. Relevant data analysis details are provided in the supporting materials (Table S3-S4, Fig. S8-S12). It was found that both mixing rules can predict the index of refraction for the polar/nonpolar tar balls, and values calculated based on “linear mixing rule” fit better with the experimental data. As mentioned above, the real fractions for polar and nonpolar BrC contributing to the mass/absorption of BBOA are undefined, some investigations report the dynamic polar BrC dominate in mass loading (50~85%), but contribute less to the absorption in BBOA (less than 40%) (Asa-Awuku et al., 2008; Bluvshtein et al., 2017; Lin et al., 2017, 2018; Rajput et al., 2014;Sengupta et al., 2018). The “linear mixing rule” confirmed in this study should be helpful in the mathematical modeling to assess climatic impacts of biomass burning related BrC aerosol, when their chemical composition is classified.

448 **3.2 Photooxidation of tar ball particles**

449 Aerosols have a wide range of atmospheric lifetimes from hours to days, during which they are involved in various
450 atmospheric processes, resulting in changes of properties (Reid et al., 2005; Rudich et al., 2007; Jimenez et al.,
451 2009). Therefore, we studied the effects of photochemical oxidation of the nonpolar wood-pyrolyzed tar ball
452 aerosols to investigate the physiochemical changes that can occur during tar balls' atmospheric lifetime. Fig. 5
453 presents the evolution of the wavelength-dependent RI and SSA as a function of the aerosols' O:C ratio following
454 NO_x-free photochemical aging in the OFR. The oxidation covers 0.7-6.7 EAD. Substantial decrease of the RI and
455 an increase of the SSA are correlated with an increase of the O:C ratio, these specific parameters are summarized
456 in Table S5 (SI). Light scattering as well as the absorption by the tar balls aerosol decrease with increasing OH
457 oxidation. The tar aerosols lose their scattering and absorption significantly up to 3.9 EAD aging. The average RI
458 decreased from initial 1.661+0.020i to 1.632+0.007i, and the corresponding average SSA increased from
459 0.89±0.01 to 0.96±0.02. Then, the RI by tar balls persisted with enhanced oxidation, so that the MAC values
460 remained stable after 3.9 days oxidation (Fig. S13, SI), suggesting that all the photochemical-labile chromophores
461 were largely eliminated, while the remaining fraction still presented some light absorption. Forrister et al. (2015)
462 also observed a stable fraction of biomass burning BrC that had persistent absorption even after long
463 photochemical evolution time in the ambient environment. They suggested that the remaining persistent fraction
464 determines the background BrC levels. In our study, the O:C ratio for tar ball aerosols increased continuously with
465 photochemical oxidation, implying production of oxygenated constituents (carboxylic, carbonyl compounds, etc.),
466 and the interaction between these increasingly oxidized species coupled with the relative stable intrinsic
467 chromophoric structures (e.g., fused aromatic rings in Fig. 3) in some supermolecular structure that may explain
468 the persistent absorption for aged tar ball aerosols (Dewar and Lepley, 1961; Desyaterik et al., 2013; Samburova
469 et al., 2016). In addition, a balance between photobleaching of intrinsic chromophores and photochemical
470 formation of BrC via gas-particle transfer, as well as dynamic gas-particle partitioning of chromophores and
471 products of their photo-degradation should also be considered in the overall absorption behavior for BBOA during
472 photochemical processes.

473 The observed photooxidation bleaching is consistent with previous studies on atmospheric processes of BrC.
474 Sumlin et al. (2017) conducted multiple-day photochemical oxidation on primary biomass burning BrC aerosols
475 and observed that BrC losses its light absorption and scattering in the near-UV wavelengths by aging. Their
476 derived RI at 375 nm decreased from 1.59+0.03i for fresh emission to 1.50+0.02i after 4.5 EAD oxidation with a

corresponding O:C ratio increase from 0.34 to 0.40. Decrease in the overall BBOA absorption and scattering was also detected *in-situ* following a one day evolution by Adler et al. (2011). They monitored an average RI of 1.53+0.07i and 1.54+0.04i for aerosols dominated by open fire and smoldering emissions, respectively, while the RI decreased to 1.49+0.02i of the aged aerosols during the following day. Zhong and Jang (2014) reported that light absorption of wood smoke BrC was modified by the photochemical process, owing to the production of BrC from SOA formation and loss of BrC from photochemical bleaching of the chromophores. The total MAC for the BrC eventually decreased by 19~68% within one day of aging. They proposed that bleaching occurred by excitation of electrons through the absorption of sunlight via π-π^* (UV and near UV illumination) or n-π^* (visible wavelengths irradiation) transitions. Then, the excited electrons disrupted the conjugated structure of chromophores, leading to the fading of wood smoke color.

When tar ball aerosols were illuminated merely by 254 nm UV light at residence time of 144s, photolysis occurred and weakly diminished their light absorption in line with the extent of photon flux exposure. UV irradiation similar to the O_3.9 condition slightly decreased the average RI to 1.649+0.018i, indicating that photolysis played a minor role in tar ball aerosols bleaching and contributed to less than 15% of imaginary k changes in NOx-free photochemical aging process. Even at full power of UV lamps in the OFR, the average RI decreased by 0.012 and 0.005i for maximum photolyzed tar balls (Table S6-S7, Fig. S14-S17, SI). As we also did not observe detectable optical changes in blank tests upon exposure to O_3 under dark (SI, Fig. S18-S19), the bleaching of the tar balls in the OFR is mainly attributed to OH-initiated chromophores decomposition via heterogeneous reactions, rather than to O_3 oxidation or photolysis.

These results indicate a fundamental relationship between photochemical processes and impairment of light absorbing and scattering abilities in tar ball aerosols. The optical behaviors of tar balls are a consequence of their chemical composition changes, which are very sensitive to photochemical process, and even one daytime atmospheric aging resulted in significant oxidation and bleaching of tar balls. In Fig. 6a, the H:C, OM/OC, $\overline{OSc}$, and particle effective density versus O:C ratio are shown. Fig. 6b presents the contributions of $C_xH_y^+$, $C_xH_yO^+$, $C_xH_yO_z^+$, and $C_xH_yO_iN_p^+$ groups to the tar balls composition under a range of OH exposure conditions. Mass spectra features and densities of the tar ball aerosols under various oxidation processes are summarized in Table S8 (SI). Increasing the OH exposure leads to continuous increase of O:C and H:C ratios, leading to higher $\overline{OSc}$ for the tar ball aerosols. This result is consistent with Sumlin et al. (2017), who reported that the O:C and H:C for BBOA increased by ~0.08 and ~0.03 after 4.5 EAD photochemical oxidation, respectively. In this work, the measured O:C ratio increased from 0.25 to 0.38 after maximum aging, while the H:C ratio increased by 0.07 from

initial value of 1.55.

Other previous studies also depicted dynamic change of elemental ratios for SOA upon aging (Aiken et al., 2008). The H:C ratio may either increase or decrease, depending on the precursor type and oxidation conditions. Overall, O:C and H:C ratios changes relate to specific chemical processes or/and to gas-particle mass transfer during aging of aerosols (Heald et al., 2010; Kim et al., 2014). The tar ball aerosols consist of mostly reduced species ($\overline{OSc}$ <0), which can be oxidized primarily via oxidative formation of polar functional groups to the carbon skeletons. In OH-initiated oxidation, functionalization includes OH/OOH function group addition and COOH:Carbonyl groups formation that increase the net oxygen content in SOA (Kroll et al., 2011). Hydration or polar functional groups addition to unsaturated C-C bonds may also increase the H:C ratio. Moreover, fragmentation or evaporation also mediate the O:C and H:C ratios of SOA in further aging (Zhang and Seinfeld, 2013; Kim et al., 2014). We attribute the increase in H:C ratio to such oxidation mechanisms that involve bulk species in the particles. As shown in Table S8 (SI), $f_{m/z>100}$ decreased monotonically with aging. After 6.7 EAD photooxidation, $f_{m/z>100}$ contributed only 21% of the total organic signals. The decrease of $f_{m/z>100}$ indicates that fragmentation reactions are involved in the photochemical evolution, and decomposition of high-molecular weight compounds, thereby, reduced the size of the conjugated molecular system. The persistent high value of $f_{m/z>100}$ after 6.7 EAD photooxidation imply that some high molecular weight compounds remained in the tar ball aerosols, and continue to contribute to light absorption ether as individual chromophores or as charge transfer complexes. From Fig. 6b, $C_xH_y^+$ fragments deplete with OH exposure, while $C_xH_yO^+$ and $C_xH_yO_z^+$ fragments increase, implying the formation of oxygenated moieties in the tar ball aerosols. In addition, a decrease in the $C_xH_yO_iN_p^+$ fraction was measured from initial 3.6% to 1.9% after the maximum oxidation. Ng et al. (2010) suggested to use $f44(CO_2^+)$ *vs.* $f43(C_2H_3O^+)$ triangle space as indication of OA sources and for estimation of their degree of oxidation and volatility. The $C_2H_3O^+$ (less oxidized fragments) is a indicative fragment from aldehydes or ketones. High *f*44/*f*43 ratio indicates low volatility and high oxidation level of SOA. Moreover, high *f*44/*f*43 and O:C ratio are associated with increased hygroscopicity and possible CCN activity of OA (Hennigan et al., 2011; Lambe et al., 2011). The *f*44 *vs.* *f*43 in this study varied with photochemical aging and fell within the expected range for ambient OOA, as shown in Fig. 7. Increase of *f*44/*f*43 ratio with OH oxidation in Fig. 6b depicted the increase of carboxylic and/or peroxide compounds compared to carbonyl species in the tar balls, which is consistent with the atmospheric evolution of ambient biomass burning plumes (Hennigan et al., 2011; Canonaco et al., 2015).

To infer the possible chemical processes, detailed mass spectras were compared between fresh and 6.7 EAD photochemical oxidized tar balls (Fig. S20, SI). We found that decrease of alkyl/alkenyl chains (e.g., $C_nH_{2n-1}^+$,

537 $C_nH_{2n+1}^+$) and aromatic ring structure fragments (e.g., $C_6H_5^+$, $C_6H_9^+$) contributed the prominent changes in the
538 $C_xH_y^+$ group, and relative higher CO_2^+ increment relative to $C_2H_3O^+$ explained the increase in the *f*44/*f*43 ratio.
539 The decrease in the abundance of $C_2H_4O_2^+$ (*m/z* 60) and $C_3H_5O_2^+$ (*m/z* 73) is consistent with recent studies that
540 levoglucosan or similar species can decay in the atmosphere due to photochemical oxidation (Hennigan et al.,
541 2010). The pronounced decrease of intensity at *m/z* 137 ($C_8H_9O_2^+$ and $C_7H_5O_3^+$) suggests that the methoxy-phenol
542 components were dissipated substantially in the aged tar balls .
543 In summary, photochemical oxidation by OH radicals destructed the aromatic rings and methoxy phenolic
544 structures, which are expected to be the primary chromophores in the tar balls. The NOC content and high-
545 molecular weight species were also depleted via OH oxidation. These chemical changes upon OH oxidation may
546 explain the observed diminishing in light scattering and absorption upon photochemical aging.

547 **3.3 NO_x-dependent tar ball particles oxidation**

548 N_2O was recently introduced for simulating NO_x-dependent SOA formation pathways in OFR under high O_3
549 concentration, as $O(^1D)+N_2O$ reactions can be applied to systematically vary the branching ratio of the RO_2+NO
550 reactions relative to the RO_2+HO_2 and/or RO_2+RO_2 reactions over a range of conditions relevant to atmospheric
551 SOA formation (Lambe et al., 2017). Here we introduced 0.5 and 2.0 vol.% N_2O to investigate NOx-involved
552 daytime aging of tar ball aerosols in the OFR. The OH exposures were maintained for all these tests at about 4
553 EAD. The corresponded NO_2 concentrations downstream of the OFR was measured to be 96.1±1.3 and 528.3±6.2
554 ppbv. The concentration of static NO can be neglected under these severe oxidation conditions. Fig. 8 shows the
555 mass spectra features for fresh and aged tar balls reacted in the absence/presence of NO_x. Parameters including
556 organic elemental ratios and densities are summarized in Table S8 (SI). In general, tar balls oxidized under N_2O
557 addition exhibit higher O:C and relative lower H:C ratios. NO_y^+ (NO^+ and NO_2^+) signals appear in the mass spectra
558 and the intensities of NO_y^+ display a positive trend with N_2O concentration, together with an increase of
559 oxygenated fragments ($C_xH_yO^+$ and $C_xH_yO_z^+$) and decrease of hydrocarbon fragments ($C_xH_y^+$). The signal ratio of
560 NO^+ (*m/z* 30) to NO_2^+ (*m/z* 46) is used to distinguish organic nitrate from inorganic nitrate. The signal from
561 standard inorganic nitrate (e.g., NH_4NO_3) has a typical NO_2^+/NO^+ ratio of 0.485 obtained from our AMS data
562 (detailed mass spectra is shown in Fig. S21, SI). The ratio and standard mass spectra are similar to previous studies
563 (Zhou et al., 2017). The fraction of NO_y^+ (NO^+ and NO_2^+) signals in the aged tar balls increased from 0% to 0.7%
564 and 1.5% at 0.5 vol.% and 2.0 vol.% N_2O additions, respectively. The corresponding values of NO_2^+/NO^+ ratio
565 are 0.162 and 0.174, which are much lower than that for inorganic nitrates. Furthermore, the contribution of

566 $C_xH_yO_iN_p^+$ fragments increased from 1.9% to 4.4% and 4.5% over the course of aging. Therefore, we can conclude
567 that NOC rather than inorganic nitrate formed in the NO_x-dependent photooxidation process, resulting in an
568 overall increase of N:C ratio from 0.010 to 0.012 and 0.015. Additionally, the density of tar balls slightly increased
569 from 1.24 for the fresh tar balls to 1.26 for the one aged in presence of 2 vol.% N_2O.

570 Detailed changes in the mass spectra over the course of the experiment are shown in Fig. S22 (SI). Indicative
571 ions of cyclolakyl fragments (e.g., $C_2H_3^+$, $C_3H_5^+$, $C_4H_7^+$) decreased, while NO_x addition increased the CO^+ and
572 CO_2^+ intensities relative to $C_2H_3O^+$, leading to higher *f*44/*f*43 ratio. Ng et al. (2007) observed a similar change for
573 photooxidation of terpenes in presence of NO_x. Changes in AMS spectra with NO_x addition may mark differences
574 between the dominating reaction pathways in tar ball photooxidation as RO_2+NO verses RO_2+HO_2 and/or
575 RO_2+RO_2 reactions.

576 Photochemical oxidation with NO_x addition enhances the oxidation level and increases both the absorption and
577 scattering of tar ball aerosols. Dynamic changes of the complex RI are shown in Fig. 9 and summarized in Table
578 S5 (SI). The RI of tar ball aerosols increased from an average of 1.632+0.007i for pure OH-initiated
579 photooxidation to 1.635+0.015i with the addition of 0.5 vol.% N_2O, and a greater increase up to 1.648+0.019i
580 with 2.0 vol.% N_2O. The increase of RI is therefore primarily attributed to NOC formation. Zhong and Jang (2014)
581 observed that higher NO_x level slowed photo-bleaching of wood smoke BrC, and they suggested that NOx-
582 modified reaction pathways produce secondary NOC chromophores (i.e., nitro-phenols). Liu et al. (2016)
583 simulated daytime chemistry of various VOCs in the presence of NOx and found that light absorption of produced
584 SOA, especially aromatic ones, increased with NOx concentration. These findings were also corroborated by
585 experimental study of Lin et al. (2015), where the chemical composition and the light absorption properties of
586 laboratory generated toluene SOA were reported to have strong positive dependence on the presence of nitro-
587 phenols formed at high NOx oxidation conditions. The color of the BrC diminished with photolysis, correlated
588 with a decline of the NOC fraction. Nitration of aromatic species via NOx/N_2O_5/NO_3 has been proposed as one
589 of the main mechanisms to produce secondary BrC in the atmosphere (Lu et al., 2011; Lin et al., 2015, 2017;
590 Bluvshtein et al., 2017).

591 The imaginary part at 2.0 vol. % N_2O addition was almost comparable with that of the fresh tar ball aerosols
592 (average value: RI=1.661+0.020*i*), although the real part was lower, suggesting that photooxidation in the
593 presence of NO_x promote the formation of N-containing chromophores via secondary processes. In our
594 experiments, formation of the N-containing chromophores overweighed the bleaching from OH photooxidation
595 to eventually regain the absorption of the aged tar balls. The average SSA calculated for 150 nm particles

596 decreased from 0.96 to 0.91 and 0.89 with N_2O addition. Absorption enhancement with N_2O addition for tar balls
597 upon photooxidation can also be seen in the MAC changes shown in Fig. S23 (SI), where MAC at 375 nm for
598 fresh tar ball was 0.854 $m^2 g^{-1}$, it decreased to 0.416 $m^2 g^{-1}$ via OH photo-bleaching, then MAC increased to 0.459
599 $m^2 g^{-1}$ at 0.5 vol.% N_2O addition, and up to 0.598 $m^2 g^{-1}$ at 2.0 vol.% N_2O addition due to chromophores formation.

600 **3.4 Atmospheric and Climate implication**

601 Atmospheric aging alters the RI of SOA, and the dynamic changes of RI depend on complicated reaction pathways
602 (Liu et al., 2016). OH-initiated photochemical oxidation and photolysis decrease the RI of laboratory proxies of
603 tar balls under NOx-free condition, while photooxidation under high NOx has an opposite effect on the RI of tar
604 balls. We investigated the relationship between the dynamic RI values of tar ball particles and their possible
605 climatic implications, including the change of light extinction/absorption efficiency and the clear-sky direct
606 radiative forcing. For clarity, light extinction/absorption efficiencies were calculated and compared at wavelength
607 of 375 and 405 nm, while radiative forcing was estimated over all the measured wavelengths from 365 to 425 nm.
608 Atmospheric and climatic implications were assessed for fresh and oxidized tar ball upon NOx-dependent ~3.9
609 EAD photooxidation (O_3.9, N_0.5, and N_2.0), in which fresh tar balls were taken as reference.

610 As shown in Fig. 10, photochemical oxidation under NOx-free condition (O_3.9) diminished light extinction
611 and absorption efficiency of tar ball aerosols in the atmospheric relevant size of 50-300 nm, causing about 5~40%
612 decrease in extinction at 375 and 405 nm wavelength. For aerosols larger than 400 nm, the extinction efficiency
613 of tar ball aerosols increased instead after photochemical aging. The light extinction efficiency presented higher
614 size-dependence than absorption, and extinction changes were more sensitive to particle size, especially in the
615 smaller sizes. The decreased absorption was more pronounced with ~60% decrease at 375 nm and over 75% at
616 405 nm. Previous studies have confirmed the relationship between biomass burning emissions and acute regional
617 visibility deterioration (Huang et al., 2012; Chen et al., 2017). Our results demonstrate that OH radical initiated
618 daytime aging may play an important role in improving visibility degradation caused by primary biomass BrC.
619 However, photochemical evolution under high NOx conditions may compensate effects of the photooxidation
620 bleaching of tar ball aerosols via the formation of NOC chromophores. At N_0.5 conditions, the light extinction
621 decreased by 4 to 20% at 375 nm and 5 to 24% at 405 nm, respectively. The corresponding absorption decrease
622 was 20~27% at both wavelengths. With more N_2O addition, formation of secondary N-containing chromophores
623 almost completely offsets light extinction/absorption decrease caused by photooxidation. Under the N_2.0
624 conditions, enhancement of light absorption efficiency for tar ball was about 0~9% at 405 nm in the entire size

range of 50-500 nm.

Radiative forcing from aerosols over both ground and snow is vital to climate models (Barnett et al., 2005; Kanakidou et al., 2005). Integrated radiative forcing for tar ball aerosols as a function of particle size under various oxidation conditions is shown in Fig. 11. Size-/wavelength-resolved SRF are also shown in Fig. S24 and S25 (SI). Integrated SRF over ground has negative values for tar balls over almost all the atmospheric relevant sizes, indicating a radiative cooling effect by tar ball aerosols except at 195~210 nm, where fresh tar ball particles present warming effect with SRF up to ~0.48 W g^{-1}. In practical fire emissions, the size of tar balls depends on the burning and environment conditions and biomass fuel types with typical values between tens to hundreds of nanometers (Reid et al., 2005; Pósfai et al., 2004). The complicated size-dependence character of SRF makes it difficult to assess the real climatic effect of tar ball particles without extensive calculations. Fig. 11a suggests fresh tar balls have SRF values of -7.46 W g^{-1} at 150 nm and 0.45 W g^{-1} at 200 nm, respectively. The SRF decreased for all size ranges due to photochemical oxidation to -7.93 W g^{-1} at 150 nm and -1.37 W g^{-1} at 200 nm for tar ball aerosols under O_3.9 condition. At N_0.5 conditions, SRF was -7.37 W g^{-1} at 150 nm and 0.16 W g^{-1} at 200 nm, and the corresponding values at N_2.0 conditions increased to -7.20 W g^{-1} at 150 nm and 0.31 W g^{-1} at 200 nm.

In contrast, tar ball particles contributed to positive forcing (warming effect) over the bright terrain throughout the atmospheric aging, as shown in Fig. 11b. Radiative forcing over the snow showed a simple increasing trend with particle size, indicating that larger BrC aerosol with identical mass loading in the air have a higher warming effect. The changes of snow-based radiative forcing upon photochemical aging followed the same trends as in the ground-based cases. Fresh tar ball at size of 200 nm has SRF of 20.12 W g^{-1} over the incident solar wavelength of 365~425 nm on the snow terrain. With photochemical oxidation under NO_x-free condition, radiative forcing decreased significantly. After 3.9 EAD atmospheric aging, snow-based radiative forcing for tar ball decreased by 65~73% over the size range of 50~500 nm, the value of 200 nm tar ball became 6.99 W g^{-1}. When NOx was involved in the photochemical oxidation of tar balls, the decrement of radiative forcing was weakened. At N_0.5, SRF for 200 nm tar ball was 14.01 W g^{-1}, while at N_2.0 condition, size-dependent SRF from the aged tar ball was almost comparable with that from fresh tar ball, and SRF for 200 nm tar ball was 18.56 W g^{-1}.

Although less than 10% of the solar spectrum's energy is distributed between 365 and 425 nm, the radiative forcing over this range represents a significant warming or cooling potential over the arctic terrain. In conclusion, photochemical oxidation under NO_x-free conditions can decrease radiative forcing of tar ball aerosols, resulting in enhancement in the cooling effect over ground and decreased in warming effect over the snow. However, NOx involvement in photooxidation inhibits the decrease in radiative forcing of tar ball aerosols. Overall, the complex

changes in optical properties of tar balls at long aging times impose great uncertainties in traditional model-based estimation of BBOA. Our study emphasizes the importance of taking this atmospheric process into consideration to refine the understanding of the climatic and atmospheric influences from these aerosols.

4 Conclusions

In this study, proxies for tar ball aerosols were generated in the laboratory following a flameless wood pyrolysis process. The optical and chemical properties of the generated tar balls were constrained using BBCES and HR-Tof-AMS/SP-LD-REMPI-MS and were shown to have many similarities to ambient biomass burning aerosols. Laboratory generated fresh tar ball aerosols have light absorption characteristics similar to atmospheric BrC with higher absorption efficiency towards the UV. The average complex refractive indices between 365 and 425 nm are 1.661+0.020i and 1.635+0.003i for nonpolar and polar tar ball aerosols, respectively.

Atmospheric evolution for tar ball aerosols was experimentally simulated using an oxidation flow reactor. The study focused on dynamic changes in the optical and chemical properties due to NOx-dependent photochemical oxidation. Furthermore, the relationship between oxidation level and the resulting RI of the tar ball aerosols was explored. We found a substantial decrease in the scattering and absorption properties of tar balls, with a corresponding increase in SSA with OH oxidation in the absence of NOx. A correlation between the RI decrease and increase in the O:C and H:C ratios was observed. The decrease in light scattering and absorption is attributed to the destruction of aromatic/phenolic/NOC and high-molecular weight species chromophores via OH-initiated photooxidation of tar balls. Over longer aging times, the average RI of the tar ball aerosols decreased from 1.661+0.020i to 1.632+0.007i upon atmospheric equivalent to 3.9 days aging, and the corresponding O:C and H:C ratio increased from initial 0.25 and 1.55 to 0.35 and 1.59, respectively.

Our results suggest that OH oxidation rather than photolysis or ozone reactions plays the dominate role that determine the optical and chemical properties in tar balls aging. The observed decrease in absorption results from depletion of chromophores such as aromatic rings, phenolic compounds and high molecular weights species.

Simulations under high NO_x environment enhanced the aerosol oxidation state and increased the scattering and absorption of tar ball aerosols relative to OH photooxidation in the absence of NOx. At ~3.9 EAD, addition of 0.5 and 2.0 vol.% N_2O increased the organic elemental ratios (O:C, H:C, and N:C ratios) and doubled the organic nitrates fraction in the particles from 1.9 % to ~4.4 %. The formation of NOC chromophores overweigh the intrinsic depletion of chromophores, leading to higher RI of 1.635+0.015i and 1.648+0.019i.

The atmospheric and climatic implications from tar ball aerosols under various oxidation conditions were

assessed using a simple radiative forcing model in terms of extinction/absorption efficiency changes and ground-/snow-based radiative forcing. These results demonstrate that the optical and chemical properties of tar ball particles are dynamically related to atmospheric aging, and optical changes are governed by both photobleaching and secondary chromophores formation. Therefore, the atmospheric process should be emphasized in model predictions for evaluating biomass burning BrC aerosol radiative forcing as well as climate change.

Acknowledgments

This research was partially supported by research grants from the US-Israel Binational Science Foundation (BSF) grant no. 2016093 and Israel Ministry of Science, Maimonide program. Dr. Li acknowledges support from the Planning & Budgeting Committee, Israel (2018/19). J. Schade, J. Passig and R. Zimmermann gratefully acknowledge financial support from the German Research Foundation, project number ZI 764/6-1, and Photonion GmbH, Schwerin, Germany.

Reference

Abo Riziq, A., Erlick, C., Dinar, E., and Rudich, Y.: Optical properties of absorbing and non-absorbing aerosols retrieved by cavity ring down (CRD) spectroscopy, Atmos. Chem. Phys., 7, 1523-1536, doi:10.5194/acp-7-1523-2007, 2007.

Adachi, K., and Buseck, P. R.: Atmospheric tar balls from biomass burning in Mexico, J. Geophys. Res. Atmos., 116, D05204, doi:10.1029/2010/2010JD015102, 2011.

Adler, G., Riziq, A. A., Erlick, C., and Rudich, Y.: Effect of intrinsic organic carbon on the optical properties of fresh diesel soot, Proc. Natl. Acad. Sci. USA, 107, 6699-6704, doi:10.1073/pnas.0903311106, 2010.

Adler, G., Flores, J. M., Abo Riziq, A., Borrmann, S., and Rudich, Y.: Chemical, physical, and optical evolution of biomass burning aerosols: a case study, Atmos. Chem. Phys., 11, 1491-1503, doi:10.5194/acp-11-1491-2011, 2011.

Aiken, A. C., Decarlo, P. F., Kroll, J. H., Worsnop, D. R., Huffman, J. A., Docherty, K. S., Ulbrich, I. M., Mohr, C., Kimmel, J. R., and Sueper, D.: O/C and OM/OC ratios of primary, secondary, and ambient organic aerosols with high-resolution time-of-flight aerosol mass spectrometry, Environ. Sci. Technol., 42, 4478-4485, doi: 10.1021/es703009q, 2008.

Alexander, D. T., Crozier, P. A., and Anderson, J. R.: Brown carbon spheres in East Asian outflow and their optical properties, Science, 321, 833-836, doi: 10.1126/science.1155296, 2008.

Andreae, M. O. and Gelencsér, A.: Black carbon or brown carbon? The nature of light-absorbing carbonaceous aerosols, Atmos. Chem. Phys., 6, 3131-3148, doi:10.5194/acp-6-3131-2006, 2006.

Asa-Awuku, A., Sullivan, A., Hennigan, C., Weber, R., and Nenes, A.: Investigation of molar volume and surfactant characteristics of water-soluble organic compounds in biomass burning aerosol, Atmos. Chem. Phys., 8, 799-812, doi:10.5194/acp-8-799-2008, 2008.

Bahadur, R., Praveen, P. S., Xu, Y., and Ramanathan, V.: Solar absorption by elemental and brown carbon determined from spectral observations, Proc. Natl. Acad. Sci. USA, 201205910, doi:10.1073/pnas.1205910109, 2012.

Barnett, T. P., Adam, J. C., and Lettenmaier, D. P.: Potential impacts of a warming climate on water availability in snow-dominated regions, Nature, 438, 303-309, doi:10.1038/nature04141, 2005.

Bente, M., Sklorz, M., Streibel, T., and Zimmermann, R.: Online laser desorption-multiphoton postionization mass spectrometry of individual aerosol particles: molecular source indicators for particles emitted from different traffic-related and wood combustion sources, Anal. Chem., 80, 8991-9004, doi:10.1021/ac801295f, 2008.

Bente, M., Sklorz, M., Streibel, T., and Zimmermann, R.: Thermal desorption-multiphoton ionization time-of-flight mass spectrometry of individual aerosol particles: A simplified approach for online single-particle analysis of Polycyclic Aromatic Hydrocarbons and their derivatives, Anal. Chem., 81, 2525-2536, doi:10.1021/ac802296f, 2009.

Bluvshtein, N., Lin, P., Flores, J. M., Segev, L., Mazar, Y., Tas, E., Snider, G., Weagle, C., Brown, S. S., and Laskin, A.: Broadband optical properties of biomass-burning aerosol and identification of brown carbon chromophores, J. Geophys. Res. Atmos. 122, 5441-5456, doi:10.1002/2016JD026230, 2017.

Boesl, U., Neusser, H., and Schlag, E.: Two-photon ionization of polyatomic molecules in a mass spectrometer, Zeitschrift für Naturforschung A, 33, 1546-1548, doi:10.1515/zna-1978-1218, 1978.

Bond, T. C., and Bergstrom, R. W.: Light absorption by carbonaceous particles: An investigative review, Aerosol Sci. Tech., 40, 27-67, doi:10.1080/02786820500421521, 2006.

Canonaco, F., Slowik, J., Baltensperger, U., and Prévôt, A.: Seasonal differences in oxygenated organic aerosol composition: implications for emissions sources and factor analysis, Atmos. Chem. Phys., 15, 6993-7002, doi:10.5194/acp-15-6993-2015, 2015.

Chakrabarty, R., Moosmüller, H., Chen, L. W., Lewis, K., Arnott, W., Mazzoleni, C., Dubey, M., Wold, C., Hao, W., and Kreidenweis, S.: Brown carbon in tar balls from smoldering biomass combustion, Atmos. Chem. Phys., 10, 6363-6370, doi:10.5194/acp-10-6363-2010, 2010.

Chen, Y., and Bond, T.: Light absorption by organic carbon from wood combustion, Atmos. Chem. Phys., 10, 1773-1787, doi:10.5194/acp-10-1773-2010, 2010.

Chen, J., Li, C., Ristovski, Z., Milic, A., Gu, Y., Islam, M. S., Wang, S., Hao, J., Zhang, H., and He, C.: A review of biomass burning: Emissions and impacts on air quality, health and climate in China, Sci. Total Environ., 579, 1000-1034, doi:10.1016/j.scitotenv.2016.11.025, 2017.

Chung, C. E., V. Ramanathan, and D. Decremer: Observationally constrained estimates of carbonaceous aerosol radiative forcing, P. Natl. Acad. Sci. USA,, 109(29), 11624-11629, doi:10.1073/pnas.1203707109, 2012.

Chýlek, P., Videen, G., Geldart, D., Dobbie, J. S., and Tso, H.: Effective medium approximations for heterogeneous particles, Light scattering by nonspherical particles: theory, measurements, and applications, 273–308, edited by: Mishchenko, M. I., Hovenier, J. W., and Travis, L. D., Academic Press, 2000.

753 Czech, H., Pieber, S. M., Tiitta, P., Sippula, O., Kortelainen, M., Lamberg, H., Grigonyte, J., Streibel, T., Prévôt,
754 A. S., and Jokiniemi, J.: Time-resolved analysis of primary volatile emissions and secondary aerosol formation
755 potential from a small-scale pellet boiler, Atmos. Environ., 158, 236-245, doi:10.1016/j.atmosenv.2017.03.040,
756 2017.
757 d'Almeida, G. A., Koepke, P., and Shettle, E. P.: Atmospheric aerosols: global climatology and radiative
758 characteristics, A. Deepak Publishing, Hampton, Va, 1991.
759 DeCarlo, P. F., Kimmel, J. R., Trimborn, A., Northway, M. J., Jayne, J. T., Aiken, A. C., Gonin, M., Fuhrer, K.,
760 Horvath, T., and Docherty, K. S.: Field-deployable, high-resolution, time-of-flight aerosol mass spectrometer,
761 Anal. Chem., 78, 8281-8289, doi:10.1021/ac061249n, 2006.
762 Desyaterik, Y., Sun, Y., Shen, X., Lee, T., Wang, X., Wang, T., and Collett, J. L.: Speciation of "brown" carbon in
763 cloud water impacted by agricultural biomass burning in eastern China, J. Geophys. Res. Atmos., 118, 7389-7399,
764 doi:10.1002/jgrd.50561, 2013.
765 Dewar, M. J., and Lepley, A. R.: π-Complexes. I. Charge Transfer Spectra of π-Complexes Formed by
766 Trinitrobenzene with Polycyclic Aromatic Compounds, J. Am. Chem. Soc., 83, 4560-4563, 1961.
767 Dinar, E., Riziq, A. A., Spindler, C., Erlick, C., Kiss, G., and Rudich, Y.: The complex refractive index of
768 atmospheric and model humic-like substances (HULIS) retrieved by a cavity ring down aerosol spectrometer
769 (CRD-AS), Faraday Discuss., 137, 279-295, doi:10.1039/B703111D, 2008.
770 Epstein, S. A., Blair, S. L., and Nizkorodov, S. A.: Direct photolysis of α-pinene ozonolysis secondary organic
771 aerosol: effect on particle mass and peroxide content, Environ. Sci. Technol., 48, 11251-11258,
772 doi:10.1021/es502350u, 2014.
773 Feng, Y., Ramanathan, V., and Kotamarthi, V.: Brown carbon: a significant atmospheric absorber of solar
774 radiation?, Atmos. Chem. Phys., 13, 8607-8621, doi:10.5194/acp-13-8607-2013, 2013.
775 Finewax, Z., de Gouw, J. A., and Ziemann, P. J.: Identification and quantification of 4-Nitrocatechol formed from
776 OH and NO_3 radical-initiated reactions of catechol in air in the presence of NOx: Implications for secondary
777 organic aerosol formation from biomass burning, Environ. Sci. Technol., 52, 1981-1989,
778 doi:10.1021/acs.est.7b05864, 2018.
779 Flores, J., Zhao, D., Segev, L., Schlag, P., Kiendler-Scharr, A., Fuchs, H., Watne, Å., Bluvshtein, N., Mentel, T.
780 F., and Hallquist, M.: Evolution of the complex refractive index in the UV spectral region in ageing secondary
781 organic aerosol, Atmos. Chem. Phys., 14, 5793-5806, doi:10.5194/acp-14-5793-2014, 2014a.

Flores, J. M., Washenfelder, R., Adler, G., Lee, H., Segev, L., Laskin, J., Laskin, A., Nizkorodov, S., Brown, S., and Rudich, Y.: Complex refractive indices in the near-ultraviolet spectral region of biogenic secondary organic aerosol aged with ammonia, Phys. Chem. Chem. Phys., 16, 10629-10642, doi:10.1039/C4CP01009D, 2014b.

Flowers, B., Dubey, M., Mazzoleni, C., Stone, E., Schauer, J., Kim, S. W., and Yoon, S.: Optical-chemical-microphysical relationships and closure studies for mixed carbonaceous aerosols observed at Jeju Island; 3-laser photoacoustic spectrometer, particle sizing, and filter analysis, Atmos. Chem. Phys., 10, 10387-10398, doi:10.5194/acp-10-10387-2010, 2010.

Forrister, H., Liu, J., Scheuer, E., Dibb, J., Ziemba, L., Thornhill, K. L., Anderson, B., Diskin, G., Perring, A. E., and Schwarz, J. P.: Evolution of brown carbon in wildfire plumes, Geophys. Res. Lett., 42, 4623-4630, doi:10.1002/2015GL063897, 2015.

Forster, P. M. F., and Taylor, K. E.: Climate forcings and climate sensitivities diagnosed from coupled climate model integrations, J. Clim., 19, 6181-6194, doi:10.1175/JCLI3974.1, 2006.

Fu, H., Zhang, M., Li, W., Chen, J., Wang, L., Quan, X., and Wang, W.: Morphology, composition and mixing state of individual carbonaceous aerosol in urban Shanghai, Atmos. Chem. Phys., 12, 693-707, doi:10.5194/acp-12-693-2012, 2012.

Ge, X., Setyan, A., Sun, Y., and Zhang, Q.: Primary and secondary organic aerosols in Fresno, California during wintertime: Results from high resolution aerosol mass spectrometry, J. Geophys. Res. Atmos., 117, D19301, doi:10.1029/2012JD018026, 2012.

Grotemeyer, J., Boesl, U., Walter, K., and Schlag, E. W.: A general soft ionization method for mass spectrometry: Resonance-enhanced multi-photon ionization of biomolecules, Org. Mass. Spectrom., 21, 645-653, doi:10.1002/oms.1210211008, 1986.

Hand, J. L., Malm, W., Laskin, A., Day, D., Lee, T. B., Wang, C., Carrico, C., Carrillo, J., Cowin, J. P., and Collett, J.: Optical, physical, and chemical properties of tar balls observed during the Yosemite Aerosol Characterization Study, J. Geophys. Res. Atmos., 110, D21210, doi:10.1029/2004JD005728, 2005.

He, L. Y., Lin, Y., Huang, X. F., Guo, S., Xue, L., Su, Q., Hu, M., Luan, S. J., and Zhang, Y. H.: Characterization of high-resolution aerosol mass spectra of primary organic aerosol emissions from Chinese cooking and biomass burning, Atmos. Chem. Phys., 10, 11535-11543, doi:10.5194/acp-10-11535-2010, 2010.

Heald, C., Kroll, J., Jimenez, J., Docherty, K., DeCarlo, P., Aiken, A., Chen, Q., Martin, S., Farmer, D., and Artaxo, P.: A simplified description of the evolution of organic aerosol composition in the atmosphere, Geophys. Res. Lett., 37, L08803, doi:10.1029/2010GL042737, 2010.

812 Hennigan, C., Miracolo, M., Engelhart, G., May, A., Presto, A., Lee, T., Sullivan, A., McMeeking, G., Coe, H.,
813 and Wold, C.: Chemical and physical transformations of organic aerosol from the photo-oxidation of open biomass
814 burning emissions in an environmental chamber, Atmos. Chem. Phys., 11, 7669-7686, doi:10.5194/acp-11-7669-
815 2011, 2011.
816 Hennigan, C. J., Sullivan, A. P., Collett Jr, J. L., and Robinson, A. L.: Levoglucosan stability in biomass burning
817 particles exposed to hydroxyl radicals, Geophys. Res. Lett., 37, L09806, doi:10.1029/2010GL043088, 2010.
818 He, Q., Bluvshtein, N., Segev, L., Meidan, D., Flores, J. M., Brown, S. S., Brune, W., and Rudich, Y.: Evolution
819 of the complex refractive index of secondary organic aerosols during atmospheric aging, Environ. Sci. Technol.,
820 52, 3456-3465, doi:10.1021/acs.est.7b05742, 2018.
821 Heger, H. J., Zimmermann, R., Dorfner, R., Beckmann, M., Griebel, H., Kettrup, A., and Boesl, U.: On-line
822 emission analysis of polycyclic aromatic hydrocarbons down to pptv concentration levels in the flue gas of an
823 incineration pilot plant with a mobile resonance-enhanced multiphoton ionization time-of-flight mass
824 spectrometer, Anal. Chem., 71, 46-57, doi:10.1021/ac980611y, 1999.
825 Herring, C. L., Faiola, C. L., Massoli, P., Sueper, D., Erickson, M. H., McDonald, J. D., Simpson, C. D., Yost, M.
826 G., Jobson, B. T., and VanReken, T. M.: New methodology for quantifying polycyclic aromatic hydrocarbons
827 (PAHs) using high-resolution aerosol mass spectrometry, Aerosol Sci. Tech., 49, 1131-1148,
828 doi:10.1080/02786826.2015.1101050, 2015.
829 Hoffer, A., Gelencsér, A., Guyon, P., Kiss, G., Schmid, O., Frank, G., Artaxo, P., and Andreae, M.: Optical
830 properties of humic-like substances (HULIS) in biomass-burning aerosols, Atmos. Chem. Phys., 6, 3563-3570,
831 doi: 10.5194/acp-6-3563-2006, 2006.
832 Hoffer, A., Tóth, A., Nyirő-Kósa, I., Pósfai, M., and Gelencsér, A.: Light absorption properties of laboratory-
833 generated tar ball particles, Atmos. Chem. Phys., 16, 239-246, doi:10.5194/acp-16-239-2016, 2016.
834 Huang, K., Zhuang, G., Fu, J. S., Wang, Q., Liu, T., Zhang, R., Jiang, Y., Deng, C., Fu, Q., and Hsu, N.: Typical
835 types and formation mechanisms of haze in an Eastern Asia megacity, Shanghai, Atmos. Chem. Phys., 12, 105-
836 124, doi:10.5194/acp-12-105-2012, 2012.
837 Huang, R. J., Yang, L., Cao, J. J., Chen, Y., Chen, Q., Li, Y., Duan, J., Zhu, C., Dai, W., and Wang, K.: Brown
838 carbon aerosol in Urban Xi'an, Northwest China: the composition and light absorption properties, Environ. Sci.
839 Technol., 52, 6825-6833, doi:10.1021/acs.est.8b02386, 2018.

IPCC. Climate Change 2013: the physical science basis. Contribution of working group I to the fifth assessment report of the intergovernmental panel on climate change. Cambridge, and New York, NY: Cambridge University Press, 2013.

Jacobson, M. Z.: Analysis of aerosol interactions with numerical techniques for solving coagulation, nucleation, condensation, dissolution, and reversible chemistry among multiple size distributions, J. Geophys. Res. Atmos., 107, D19, 4366, doi:10.1029/2001JD002044, 2002.

Jacobson, M. Z.: Investigating cloud absorption effects: Global absorption properties of black carbon, tar balls, and soil dust in clouds and aerosols, J. Geophys. Res. Atmos., 117(D6), doi:10.1029/2011ID017218, 2012.

Jacobson, M. Z.: Effects of biomass burning on climate, accounting for heat and moisture fluxes, black and brown carbon, and cloud absorption effects, J. Geophys. Res. Atmos., 119, 8980-9002, doi.org/10.1002/2014JD021861, 2014.

Jimenez, J., Canagaratna, M., Donahue, N., Prevot, A., Zhang, Q., Kroll, J. H., DeCarlo, P. F., Allan, J. D., Coe, H., and Ng, N.: Evolution of organic aerosols in the atmosphere, Science, 326, 1525-1529, doi: 10.1126/science.1180353, 2009.

Jo, D. S., Park, R. J., Lee, S., Kim, S. W., and Zhang, X.: A global simulation of brown carbon: implications for photochemistry and direct radiative effect, Atmos. Chem. Phys., 16, 3413-3432, doi:10.5194/acp-16-3413-2016, 2016.

Kanakidou, M., Seinfeld, J., Pandis, S., Barnes, I., Dentener, F., Facchini, M., Dingenen, R. V., Ervens, B., Nenes, A., and Nielsen, C.: Organic aerosol and global climate modelling: a review, Atmos. Chem. Phys., 5, 1053-1123, doi: 1680-7324/acp/2005-5-1053, 2005.

Kang, E., Root, M., Toohey, D., and Brune, W.: Introducing the concept of potential aerosol mass (PAM), Atmos. Chem. Phys., 7, 5727-5744, doi: 10.5194/acp-7-5727-2007, 2007.

Kim, H., Liu, S., Russell, L. M., and Paulson, S. E.: Dependence of real refractive indices on O:C, H:C and mass fragments of secondary organic aerosol generated from ozonolysis and photooxidation of limonene and α-pinene, Aerosol Sci. Tech., 48, 498-507, doi: 10.1080/02786826.2014.893278, 2014.

Kroll, J. H., Donahue, N. M., Jimenez, J. L., Kessler, S. H., Canagaratna, M. R., Wilson, K. R., Altieri, K. E., Mazzoleni, L. R., Wozniak, A. S., and Bluhm, H.: Carbon oxidation state as a metric for describing the chemistry of atmospheric organic aerosol, Nat. Chem., 3, 133, doi: 10.1038/NCHEM.948, 2011.

Lack, D. A., Langridge, J. M., Bahreini, R., Cappa, C. D., Middlebrook, A. M., and Schwarz, J. P.: Brown carbon and internal mixing in biomass burning particles, Proc. Natl. Acad. Sci. USA, 109, 14802-14807, doi:10.1073/pnas.1206575109, 2012.

Lambe, A., Onasch, T., Massoli, P., Croasdale, D., Wright, J., Ahern, A., Williams, L., Worsnop, D., Brune, W., and Davidovits, P.: Laboratory studies of the chemical composition and cloud condensation nuclei (CCN) activity of secondary organic aerosol (SOA) and oxidized primary organic aerosol (OPOA), Atmos. Chem. Phys., 11, 8913-8928, doi:10.5194/acp-11-8913-2011, 2011.

Lambe, A., Massoli, P., Zhang, X., Canagaratna, M., Nowak, J., Daube, C., Chao, Y., Nie, W., Onasch, T., and Jayne, J.: Controlled nitric oxide production via O (^{1}D)+ N_2O reactions for use in oxidation flow reactor studies, Atmos. Meas. Tech., 10, 2283, doi: 10.5194/amt-10-2283-2017, 2017.

Laskin, A., Laskin, J., and Nizkorodov, S. A.: Chemistry of atmospheric brown carbon, Chem. Rev., 115, 4335-4382, doi:10.1021/cr5006167, 2015.

Laskin, A., Smith, J. S., and Laskin, J.: Molecular characterization of nitrogen-containing organic compounds in biomass burning aerosols using high-resolution mass spectrometry, Environ. Sci. Technol., 43, 3764-3771, doi:10.1021/es803456n, 2009.

Lee, H. J., Aiona, P. K., Laskin, A., Laskin, J., and Nizkorodov, S. A.: Effect of solar radiation on the optical properties and molecular composition of laboratory proxies of atmospheric brown carbon, Environ. Sci. Technol., 48, 10217-10226, doi:10.1021/es502515r, 2014.

Levinson, R., Akbari, H., and Berdahl, P.: Measuring solar reflectance-Part I: Defining a metric that accurately predicts solar heat gain, Sol. Energy, 84, 1717-1744, doi:10.1016/j.solener.2010.04.018, 2010.

Li, C., Ma, Z., Chen, J., Wang, X., Ye, X., Wang, L., Yang, X., Kan, H., Donaldson, D., and Mellouki, A.: Evolution of biomass burning smoke particles in the dark, Atmos. Environ., 120, 244-252, doi:10.1016/j.atmosenv.2015.09.003, 2015.

Li, C., Hu, Y., Zhang, F., Chen, J., Ma, Z., Ye, X., Yang, X., Wang, L., Tang, X., and Zhang, R.: Multi-pollutant emissions from the burning of major agricultural residues in China and the related health-economic effects, Atmos. Chem. Phys., 17, 4957-4988, doi:10.5194/acp-17-4957-2017, 2017.

Li, Y., Huang, D., Cheung, H. Y., Lee, A., and Chan, C. K.: Aqueous-phase photochemical oxidation and direct photolysis of vanillin-a model compound of methoxy phenols from biomass burning, Atmos. Chem. Phys., 14, 2871-2885, doi:10.5194/acp-14-2871-2014, 2014.

Li, Y. J., Yeung, J. W., Leung, T. P., Lau, A. P., and Chan, C. K.: Characterization of organic particles from incense burning using an aerodyne high-resolution time-of-flight aerosol mass spectrometer, Aerosol Sci. Tech., 46, 654-665, doi:10.1080/02786826.2011.653017, 2012.

Lin, P., Liu, J., Shilling, J. E., Kathmann, S. M., Laskin, J., and Laskin, A.: Molecular characterization of brown carbon (BrC) chromophores in secondary organic aerosol generated from photo-oxidation of toluene, Phys. Chem. Chem. Phys., 17, 23312-23325, doi:10.1039/C5CP02563J, 2015.

Lin, P., Aiona, P. K., Li, Y., Shiraiwa, M., Laskin, J., Nizkorodov, S. A., and Laskin, A.: Molecular characterization of brown carbon in biomass burning aerosol particles, Environ. Sci. Technol., 50, 11815-11824, doi:10.1021/acs.est.6b03024, 2016.

Lin, P., Bluvshtein, N., Rudich, Y., Nizkorodov, S. A., Laskin, J., and Laskin, A.: Molecular Chemistry of Atmospheric Brown Carbon Inferred from a Nationwide Biomass Burning Event, Environ. Sci. Technol., 51, 11561-11570, doi:10.1021/acs.est.7b02276, 2017.

Lin, P., Fleming, L. T., Nizkorodov, S. A., Laskin, J., and Laskin, A.: Comprehensive Molecular Characterization of Atmospheric Brown Carbon by High Resolution Mass Spectrometry with Electrospray and Atmospheric Pressure Photoionization, Anal. chem., 90, 12493-12502, doi:10.1021/acs.analchem.8b02177, 2018.

Liu, J., Bergin, M., Guo, H., King, L., Kotra, N., Edgerton, E., and Weber, R.: Size-resolved measurements of brown carbon in water and methanol extracts and estimates of their contribution to ambient fine-particle light absorption, Atmos. Chem. Phys., 13, 12389-12404, doi:10.5194/acp-13-12389-2013, 2013.

Liu, J., Lin, P., Laskin, A., Laskin, J., Kathmann, S. M., Wise, M., Caylor, R., Imholt, F., Selimovic, V., and Shilling, J. E.: Optical properties and aging of light-absorbing secondary organic aerosol, Atmos. Chem. Phys., 16, 12815-12827, doi:10.5194/acp-16-12815-2016, 2016.

Lu, J. W., Flores, J. M., Lavi, A., Abo-Riziq, A., and Rudich, Y.: Changes in the optical properties of benzo[a] pyrene-coated aerosols upon heterogeneous reactions with NO_2 and NO_3, Phys. Chem. Chem. Phys., 13, 6484-6492, doi:10.1039/C0CP02114H, 2011.

McDonald, J. D., Zielinska, B., Fujita, E. M., Sagebiel, J. C., Chow, J. C., and Watson, J. G.: Fine particle and gaseous emission rates from residential wood combustion, Environ. Sci. Technol., 34, 2080-2091, doi:10.1021/es9909632, 2000.

Moise, T., Flores, J. M., and Rudich, Y.: Optical properties of secondary organic aerosols and their changes by chemical processes, Chem. Rev., 115, 4400-4439, doi:10.1021/cr5005259, 2015.

Miljevic, B., Hedayat, F., Stevanovic, S., Fairfull-Smith, K. E., Bottle, S., and Ristovski, Z.: To sonicate or not to sonicate PM filters: reactive oxygen species generation upon ultrasonic irradiation, Aerosol Sci. Tech., 48, 1276-1284, doi:10.1080/02786826.2014.981330, 2014.

Mutzel, A., Rodigast, M., Iinuma, Y., Böge, O., and Herrmann, H.: An improved method for the quantification of SOA bound peroxides, Atmos. Environ., 67, 365-369, doi:10.1016/j.atmosenv.2012.11.012, 2013.

Ng, N., Chhabra, P., Chan, A., Surratt, J. D., Kroll, J., Kwan, A., McCabe, D., Wennberg, P., Sorooshian, A., and Murphy, S.: Effect of NOx level on secondary organic aerosol (SOA) formation from the photooxidation of terpenes, Atmos. Chem. Phys., 7, 5159-5174, doi:10.5194/acp-7-5159-2007, 2007.

Ng, N., Canagaratna, M., Zhang, Q., Jimenez, J., Tian, J., Ulbrich, I., Kroll, J., Docherty, K., Chhabra, P., and Bahreini, R.: Organic aerosol components observed in Northern Hemispheric datasets from Aerosol Mass Spectrometry, Atmos. Chem. Phys., 10, 4625-4641, doi:10.5194/acp-10-4625-2010, 2010.

Ng, N., Canagaratna, M., Jimenez, J., Chhabra, P., Seinfeld, J., and Worsnop, D.: Changes in organic aerosol composition with aging inferred from aerosol mass spectra, Atmos. Chem. Phys., 11, 6465-6474, doi:10.5194/acp-11-6465-2011, 2011.

Park, R. J., Kim, M. J., Jeong, J. I., Youn, D., and Kim, S.: A contribution of brown carbon aerosol to the aerosol light absorption and its radiative forcing in East Asia, Atmos. Environ., 44, 1414-1421, doi:10.1016/j.atmosenv.2010.01.042, 2010.

Passig, J., Schade, J., Oster, M., Fuchs, M., Ehlert, S., Jäger, C., Sklorz, M., and Zimmermann, R.: Aerosol mass spectrometer for simultaneous detection of polyaromatic hydrocarbons and inorganic components from individual particles, Anal. Chem., 89, 6341-6345, doi:10.1021/acs.analchem.7b01207, 2017.

Peng, Z., Day, D., Stark, H., Li, R., Lee-Taylor, J., Palm, B., Brune, W., and Jimenez, J. L.: HOx radical chemistry in oxidation flow reactors with low-pressure mercury lamps systematically examined by modeling, Atmos. Meas. Tech., 8, 4863-4890, doi:10.5194/amt-8-4863-2015, 2015.

Peng, Z., Day, D. A., Ortega, A. M., Palm, B. B., Hu, W., Stark, H., Li, R., Tsigaridis, K., Brune, W. H., and Jimenez, J. L.: Non-OH chemistry in oxidation flow reactors for the study of atmospheric chemistry systematically examined by modeling, Atmos. Chem. Phys., 16, 4283-4305, doi:10.5194/acp-16-4283-2016, 2016.

Peng, Z., and Jimenez, J. L.: Modeling of the chemistry in oxidation flow reactors with high initial NO, Atmos. Chem. Phys., 17, 11991-12010, doi:10.5194/acp-17-11991-2017, 2017.

954 Pettersson, A., Lovejoy, E. R., Brock, C. A., Brown, S. S., and Ravishankara, A.: Measurement of aerosol optical
955 extinction at 532 nm with pulsed cavity ring down spectroscopy, J. Aerosol Sci., 35, 995-1011,
956 doi:10.1016/j.jaerosci.2004.02.008, 2004.
957 Phillips, S. M., and Smith, G. D.: Light absorption by charge transfer complexes in brown carbon aerosols,
958 Environ. Sci. Technol.. Lett., 1, 382-386, doi:10.1021/ez500263j, 2014.
959 Pósfai, M., Gelencsér, A., Simonics, R., Arató, K., Li, J., Hobbs, P. V., and Buseck, P. R.: Atmospheric tar balls:
960 Particles from biomass and biofuel burning, J. Geophys. Res. Atmos., 109, D06213, doi:10.1029/2003JD004169,
961 2004.
962 Rajput, P., and Sarin, M.: Polar and non-polar organic aerosols from large-scale agricultural-waste burning
963 emissions in Northern India: implications to organic mass-to-organic carbon ratio, Chemosphere, 103, 74-
964 79, doi:10.1016/j.chemosphere.2013.11.028, 2014.
965 Reid, J. S., Eck, T. F., Christopher, S. A., Koppmann, R., Dubovik, O., Eleuterio, D., Holben, B. N., Reid, E. A.,
966 and Zhang, J.: A review of biomass burning emissions part III: intensive optical properties of biomass burning
967 particles, Atmos. Chem. Phys., 5, 827-849, doi:10.5194/acp-5-827-2005, 2005.
968 Rettner, C. T., and Brophy, J. H.: Resonance enhanced laser ionisation mass spectrometry of four aromatic
969 molecules, Chem. Phys., 56, 53-61, doi:10.1016/0301-0104(81)85099-9, 1981.
970 Rollins, A. W., Browne, E. C., Min, K. E., Pusede, S. E., Wooldridge, P. J., Gentner, D. R., Goldstein, A. H., Liu,
971 S., Day, D. A., and Russell, L. M.: Evidence for NOx control over nighttime SOA formation, Science, 337, 1210-
972 1212, doi:10.1126/science.1221520, 2012.
973 Rudich, Y., Donahue, N. M., and Mentel, T. F.: Aging of organic aerosol: Bridging the gap between laboratory
974 and field studies, Annu. Rev. Phys. Chem., 58, 321-352, doi:10.1146/annurev.physchem.58.032806.104432, 2007.
975 Russell, P., Bergstrom, R., Shinozuka, Y., Clarke, A., DeCarlo, P., Jimenez, J., Livingston, J., Redemann, J.,
976 Dubovik, O., and Strawa, A.: Absorption Ångström Exponent in AERONET and related data as an indicator of
977 aerosol composition, Atmos. Chem. Phys., 10, 1155-1169, doi:10.5194/acp-10-1155-2010, 2010.
978 Samburova, V., Connolly, J., Gyawali, M., Yatavelli, R. L., Watts, A. C., Chakrabarty, R. K., Zielinska, B.,
979 Moosmüller, H., and Khlystov, A.: Polycyclic aromatic hydrocarbons in biomass-burning emissions and their
980 contribution to light absorption and aerosol toxicity, Sci. Total Environ., 568, 391-401,
981 doi:10.1016/j.scitotenv.2016.06.026, 2016.

Schauer, J. J., Kleeman, M. J., Cass, G. R., and Simoneit, B. R.: Measurement of emissions from air pollution sources. 3. C1-C29 organic compounds from fireplace combustion of wood, Environ. Sci. Technol., 35, 1716-1728, doi:10.1021/es001331e, 2001.

Sedlacek III, A. J., Buseck, P. R., Adachi, K., Onasch, T. B., Springston, S. R., and Kleinman, L.: Formation and evolution of Tar Balls from Northwestern US wildfires, Atmos. Chem. Phys., 18, 11289-11301, doi:10.5194/acp-18-11289-2018, 2018.

Seinfeld, J. H., and Pandis, S. N.: Atmospheric chemistry and physics: from air pollution to climate change, 3rd edition, John Wiley & Sons, Inc., Hoboken, New Jersey, USA, 2016.

Sengupta, D., Samburova, V., Bhattarai, C., Kirillova, E., Mazzoleni, L., Iaukea-Lum, M., Watts, A., Moosmüller, H., and Khlystov, A.: Light absorption by polar and non-polar aerosol compounds from laboratory biomass combustion, Atmos. Chem. Phys., 18, 10849-10867, doi:10.5194/acp-18-10849-2018, 2018.

Shamjad, P. M., Satish, R. V., Thamban, N. M., Rastogi, N., and Tripathi, S.: Absorbing refractive index and direct radiative forcing of atmospheric Brown Carbon over Gangetic Plain, ACS Earth Space Chem., 2, 31-37, doi:10.1021/acsearthspacechem.7b00074, 2018.

Shen, G., Tao, S., Wei, S., Zhang, Y., Wang, R., Wang, B., Li, W., Shen, H., Huang, Y., and Yang, Y.: Retene emission from residential solid fuels in China and evaluation of retene as a unique marker for soft wood combustion, Environ. Sci. Technol., 46, 4666-4672, doi:10.1021/es300144m, 2012.

Shen, H., Huang, Y., Wang, R., Zhu, D., Li, W., Shen, G., Wang, B., Zhang, Y., Chen, Y., and Lu, Y.: Global atmospheric emissions of polycyclic aromatic hydrocarbons from 1960 to 2008 and future predictions, Environ. Sci. Technol., 47, 6415-6424, doi:10.1021/es400857z, 2013.

Shrivastava, M., Cappa, C. D., Fan, J., Goldstein, A. H., Guenther, A. B., Jimenez, J. L., Kuang, C., Laskin, A., Martin, S. T., and Ng, N. L.: Recent advances in understanding secondary organic aerosol: Implications for global climate forcing, Rev. Geophys., 55, 509-559, doi:10.1002/2016RG000540, 2017.

Sigsgaard, T., Forsberg, B., Annesi-Maesano, I., Blomberg, A., Bølling, A., Boman, C., Bønløkke, J., Brauer, M., Bruce, N., and Héroux, M. E.: Health impacts of anthropogenic biomass burning in the developed world, Eur. Respir. J., 46, 1577-1588, doi:10.1183/13993003.01865-2014, 2015.

Sumlin, B. J., Pandey, A., Walker, M. J., Pattison, R. S., Williams, B. J., and Chakrabarty, R. K.: Atmospheric Photooxidation Diminishes Light Absorption by Primary Brown Carbon Aerosol from Biomass Burning, Environ. Sci. Technol. Lett., 4, 540-545, doi:10.1021/acs.estlett.7b00393, 2017.

1012 Sumlin, B. J., Oxford, C. R., Seo, B., Pattison, R. R., Williams, B. J., and Chakrabarty, R. K.: Density and
1013 homogeneous internal composition of primary brown carbon aerosol, Environ. Sci. Technol., 52, 3982-3989, doi:
1014 10.1021/acs.est.8b00093, 2018.
1015 Tavakoli, F., and Olfert, J.: An instrument for the classification of aerosols by particle relaxation time: theoretical
1016 models of the aerodynamic aerosol classifier, Aerosol Sci. Tech., 47, 916-926,
1017 doi:10.1080/02786826.2013.802761, 2013.
1018 Tavakoli, F., and Olfert, J. S.: Determination of particle mass, effective density, mass-mobility exponent, and
1019 dynamic shape factor using an aerodynamic aerosol classifier and a differential mobility analyzer in tandem, J.
1020 Aerosol Sci., 75, 35-42, doi:10.1016/j.jaerosci.2014.04.010, 2014.
1021 Tóth, A., Hoffer, A., Nyirő-Kósa, I., Pósfai, M., and Gelencsér, A.: Atmospheric tar balls: aged primary droplets
1022 from biomass burning?, Atmos. Chem. Phys., 14, 6669-6675, doi:10.5194/acp-14-6669-2014, 2014.
1023 Washenfelder, R., Attwood, A., Brock, C., Guo, H., Xu, L., Weber, R., Ng, N., Allen, H., Ayres, B., and Baumann,
1024 K.: Biomass burning dominates brown carbon absorption in the rural southeastern United States, Geophys. Res.
1025 Lett., 42, 653-664, doi:10.1002/2014GL062444, 2015.
1026 Washenfelder, R., Flores, J., Brock, C., Brown, S., and Rudich, Y.: Broadband measurements of aerosol extinction
1027 in the ultraviolet spectral region, Atmos. Meas. Tech., 6, 861-877, doi:10.5194/amt-6-861-2013, 2013.
1028 Wei, C., Bandowe, B. A. M., Han, Y., Cao, J., Zhan, C., and Wilcke, W.: Polycyclic aromatic hydrocarbons (PAHs)
1029 and their derivatives (alkyl-PAHs, oxygenated-PAHs, nitrated-PAHs and azaarenes) in urban road dusts from
1030 Xi'an, Central China, Chemosphere, 134, 512-520, doi:10.1016/j.chemosphere.2014.11.052, 2015.
1031 Weimer, S., Alfarra, M., Schreiber, D., Mohr, M., Prévôt, A., and Baltensperger, U.: Organic aerosol mass spectral
1032 signatures from wood-burning emissions: Influence of burning conditions and wood type, J. Geophys. Res.
1033 Atmos., 113, doi:10.1029/2007JD009309, 2008.
1034 Wong, J. P., Zhou, S., and Abbatt, J. P.: Changes in secondary organic aerosol composition and mass due to
1035 photolysis: relative humidity dependence, J. Phys. Chem. A, 119, 4309-4316, doi:10.1021/jp506898c, 2014.
1036 Xie, M., Hays, M. D., and Holder, A. L.: Light-absorbing organic carbon from prescribed and laboratory biomass
1037 burning and gasoline vehicle emissions, Scientific Reports, 7, 7318, doi:10.1038/s41598-017-06981-8, 2017.
1038 Yee, L., Kautzman, K., Loza, C., Schilling, K., Coggon, M., Chhabra, P., Chan, M., Chan, A., Hersey, S., and
1039 Crounse, J.: Secondary organic aerosol formation from biomass burning intermediates: phenol and
1040 methoxyphenols, Atmos. Chem. Phys., 13, 8019-8043, doi:10.5194/acp-13-8019-2013, 2013.

1041 Yu, L., Smith, J., Laskin, A., Anastasio, C., Laskin, J., and Zhang, Q.: Chemical characterization of SOA formed
1042 from aqueous-phase reactions of phenols with the triplet excited state of carbonyl and hydroxyl radical, Atmos.
1043 Chem. Phys., 14, 13801-13816, doi:10.5194/acp-14-13801-2014, 2014.
1044 Zhang, H., and Ying, Q.: Secondary organic aerosol from polycyclic aromatic hydrocarbons in Southeast Texas,
1045 Atmos. Environ., 55, 279-287, doi:10.1016/j.atmosenv.2012.03.043, 2012.
1046 Zhang, X., and Seinfeld, J.: A functional group oxidation model (FGOM) for SOA formation and aging, Atmos.
1047 Chem. Phys., 13, 5907-5926, doi:10.5194/acp-14-13801-2014, 2013.
1048 Zhong, M., and Jang, M.: Dynamic light absorption of biomass-burning organic carbon photochemically aged
1049 under natural sunlight, Atmos. Chem. Phys., 14, 1517-1525, doi:10.5194/acp-14-1517-2014, 2014.
1050 Zhou, S., Collier, S., Jaffe, D. A., Briggs, N. L., Hee, J., Sedlacek III, A. J., Kleinman, L., Onasch, T. B., and
1051 Zhang, Q.: Regional influence of wildfires on aerosol chemistry in the western US and insights into atmospheric
1052 aging of biomass burning organic aerosol, Atmos. Chem. Phys., 17, 2477-2493, doi:10.5194/acp-17-2477-2017,
1053 2017.
1054

Caption of Table and Figure

Table 1. Experimental conditions for tar balls photochemical oxidation

Table 2. Comparison of tar ball particle optical parameters with reference values of BBOA (mean ± standard deviation)

Figure 1. Experimental setup for laboratory generation and aging of tar ball aerosol: including generation setup, OFR photochemical aging, gaseous-particulate chemical monitoring, particle size distribution and optical properties measurements.

Figure 2. High-resolution AMS mass spectra of fresh polar and nonpolar tar ball particles. Four ion groups are grouped for clarity as: $C_xH_y^+$ (green), $C_xH_yO^+$ (purple), $C_xH_yO_z^+$ (z>1) (violet), $C_xH_yO_iN_p^+$(i≧0, p≧1) (light blue). The mass fractions of the four fragment groups are presented by pie-charts.

Figure 3. LD-REMPI mass spectra of exemplary single tar ball particles, some feature peaks were identified and labeled. a) Nonpolar tar ball spectra shows predominantly alkyl-substituted and unsubstituted PAHs. b) Polar tar ball spectra reveals many oxidized aromatics, e.g., methoxy-phenol, benzenediol. Note the softwood combustion marker retene at *m/z*=234, its characteristic fragments (*m/z*=203, 204, 205, 219) and possible retene derivatives (*m/z*=248, 250).

Figure 4. Wavelength-dependent RI and SSA for tar ball particles generated from polar, nonpolar and mixture of the two phases tarry solutions (only retrieval for mixture of 1:1 in vol. is shown for clarity, optical results for the rest two mixtures can be found in supporting materials). The shaded areas indicate the upper and lower limits of the imaginary part calculated from UV-Vis spectra of methanol extracts from the corresponding tar ball particles samples: a) real part, b) imaginary part, and c) SSA calculated for 150 nm particles. Overplayed in green symbol are previous measurements of biomass burning from the literature.

Figure 5. Evolution of the retrieved wavelength-dependent complex RI and SSA as a function of O:C ratio for tar ball particles upon OH photochemical oxidation: a) real part, b) imaginary part, and c) SSA calculated for 150 nm particles. The color scale shows the span in the RI for the wavelengths measured from 365 to 425 nm. For clarity, error bars for O:C ratio (±0.01), RI (±0.007 for real part, and ±0.003 for imaginary part on average), and SSA (±0.006) are not shown. Two dashed lines trace the RI and SSA at 375 nm (purple) and 405 nm (green). O_0.7~O_6.7 represent equivalent atmospheric photochemical oxidation for 0.7 and up to 6.7 days.

Figure 6. Dynamic changes for the chemical characteristics of tar ball particle under NOx-free OH photochemical oxidation: a) OM/OC, H:C ratio, particle density, and average carbon oxidation state ($\overline{OSc}$) changes as a function

of O:C ratio; b) mass spectra evolution with oxidation times in term of $C_xH_y^+$, $C_xH_yO^+$, $C_xH_yO_z^+$, and $C_xH_yO_iN_p^+$ fragment groups.

Figure 7. Comparison of *f*44 and *f*43 values from ambient data sets (Ng. et al., 2010) and values from ambient biomass burning organic aerosol.

Figure 8. Dynamic changes for chemical characteristics of tar ball aerosols under NO_x-dependent OH photochemical oxidation: a) OM/OC, O:C, H:C, and particle density changes; b) mass spectra changes with different oxidation conditions in term of $C_xH_y^+$, $C_xH_yO^+$, $C_xH_yO_z^+$, and $C_xH_yO_zN_p^+$ fragment groups. $C_xH_yO_zN_p^+$ include all nitrogen-containing fragments, (e.g., $C_xH_yON^+$, $C_xH_yO_zN_i^+$, $C_xH_yN^+$, etc.), NO_y^+ include NO^+ and NO_2^+. O_3.9 represents 3.9 days equivalent atmospheric photochemical aging in absence of NOx, N_0.5 and N_2.0 indicate photochemical oxidation with 0.5 and 2.0 vol.% N_2O addition at ~4.0 days atmospheric oxidation.

Figure 9. Changes of retrieved spectra-dependent RI as a function of O:C ratio for tar ball particles upon NOx-dependent photochemical oxidation: a) real part, b) imaginary part, and c) SSA calculated from 150 nm particles. For clarity, error bars for O:C ratio (±0.01), RI (±0.006 for real part, and ±0.003 for imaginary part on average), and SSA (±0.007) are not shown.O_3.9 represents 3.9 days equivalent atmospheric photochemical aging in absence of NOx, N_0.5 and N_2.0 indicate photochemical oxidation with 0.5 and 2.0 vol.% N_2O addition at ~4.0 days atmospheric oxidation.

Figure 10. Size-resolved light extinction and absorption efficiency ratio of NO_x-dependent photooxidized tar balls compared to the fresh tar ball particles: a) and c) extinction ratios at 375 and 405 nm, b) and d) absorption ratios at 375 and 405 nm. O_3.9 represents 3.9 days equivalent atmospheric photochemical aging in absence of NOx, N_0.5 and N_2.0 indicate photochemical oxidation with 0.5 and 2.0 vol.% N_2O addition at ~4.0 days atmospheric oxidation.

Figure 11. Calculated size-resolved simple radiative forcing (SRF, W g^{-1}) by tar ball aerosols, integrated over 365~425 nm incident solar irradiation for fresh and NOx-dependent photooxidized tar balls: a) ground-based radiative forcing, b) snow-based radiative forcing.

1108 **Table 1**. Experimental conditions for tar ball particles photochemical oxidation

Experiment	O_3 (ppm)	N_2O mixing ratio	Endpoint NO_x (ppb)	RH (%)	water mixing ratio	Exposure	
						OH radical (molecules cm^{-3} s)	photon flux (photons cm^{-2})
P1	——	——	——	38.90	0.0126	——	7.47E+15
P2	——	——	——	39.70	0.0128	——	4.83E+16
P3	——	——	——	40.50	0.0130	——	1.00E+17
O_0.7	24.46	——	——	37.29	0.0120	8.68E+10	1.56E+15
O_1.7	24.76	——	——	37.66	0.0122	2.23E+11	7.47E+15
O_3.9	24.63	——	——	35.58	0.0115	5.11E+11	4.83E+16
O_6.7	25.31	——	——	35.67	0.0116	8.65E+11	5.17E+16
N_0.5	24.18	0.005	96.1	36.60	0.0118	5.37E+11	5.92E+16
N_2.0	28.21	0.020	528.3	35.90	0.0116	4.85E+11	1.00E+17

1109 Note: P1~P3 mean photolysis test, O_0.7~O_6.7 correspond to photochemical oxidation experiment from equivalent 0.7 day to 6.7 days
1110 ageing, and N_0.5 and N_2.0 indicate photochemical oxidation with N_2O addition at 0.5 vol.% and 2 vol.% mixing ratios (standard deviation
1111 for the parameters were not given in above table)

Table 2. Compare of tar ball particle optical properties with reference values of BBOA (mean ± standard deviation)

BrC	Complex Refractive index			$Å_{abs}$	$Å_{abs\_UVVIS}$	$Å_{ext}$	Reference
	Average	375nm	405nm				
Nonpolar	(1.661±0.008)+(0.020±0.004)i	(1.671±0.003)+(0.025±0.003)i	(1.659±0.011)+(0.017±0.002)i	5.87 ± 0.37	5.74	3.81 ± 0.18	This work
Mixture (2:1 in vol.)	(1.670±0.010)+(0.017±0.004)i	(1.682±0.008)+(0.021±0.002)i	(1.668±0.007)+(0.013±0.001)i	6.79 ± 0.91	7.08	4.01 ± 0.09	
Mixture (1:1 in vol.)	(1.694±0.011)+(0.013±0.003)i	(1.703±0.015)+(0.017±0.001)i	(1.689±0.011)+(0.009±0.002)i	6.16 ± 0.54	7.38	3.73 ± 0.23	
Mixture (1:2 in vol.)	(1.672±0.010)+(0.011±0.004)i	(1.683±0.005)+(0.018±0.002)i	(1.667±0.003)+(0.006±0.003)i	6.66 ± 0.63	7.24	4.06 ± 0.11	
Polar	(1.635±0.009)+(0.003±0.003)i	(1.647±0.003)+(0.005±0.001)i	(1.635±0.004)+(0.004±0.003)i	6.72 ± 2.28 [a]	7.83	3.93 ± 0.06	
BBOA	1.590+0.029i@375nm, 1.570+0.010i@405nm (IPN)			6.4~7.4			Sumlin et al., 2017; 2018
BBOA	1.590+0.017i@405nm (IPN)						Flowers et al., 2010
BBOA	*k*: 0.009@404nm (CRDS-PAS)						Lack et al., 2012
Tar ball	1.78+0.015i, 1.83+0.0086i@405nm (IPN)			4.2~6.4			Chakrabarty et al., 2010
Tar ball	1.56+0.02i @405nm (CRDS-UVVIS)						Hand et al., 2005
BBOA	1.53+0.07i (WELAS,open fire), 1.54+0.04i (WELAS, smoldering)						Adler et al., 2011
BBOA	1.64+0.03i@405nm (BBCES-Neph)			4~6 [b]		2~3 [b]	Bluvshtein et al., 2017
BBOA_HULIS	1.653+0.002i, 1.685+0.002i@532nm(Nep-PAS)				6~7		Hoffer et al., 2006
BBOA_HULIS	1.616+0.023i@390nm(CRDS)						Dinar et al., 2008
BBOA	1.550+0.033i@365nm (BBCES)						Washenfelder et al., 2015
BBOA					6.9~11.4 [c]		Chen and Bond, 2010
BBOA					5.3~8.1 [c]		Xie et al., 2017
Ambient SOA					6.0~6.3 [c]		Huang et al., 2018
Ambient SOA	*k*: 0.046@365nm, 0.039@405nm, 0.036@420nm (LWCC)						Shamjad et al., 2018

Note: $Å_{abs}$ and $Å_{ext}$ were calculated form tar ball particle with median diameter of 150 nm in this study

[a] regressed over wavelength range of 365~400 nm, no absorption detected over 410 nm using BBCES system

[b] regressed over wavelength range of 300~650 nm for bulk fire plume emissions

[c] $Å_{abs\_UVVIS}$ of methanol extracts over whole range from 300/360~600 nm

Instrument: IPN(integrated photoacoustic nephelometer), CRDS (cavity ring-down spectrometer), PAS (photoacoustic absorption spectrometer), WELAS (white light optical particle counter), LWCC (a liquid waveguide capillary cell)

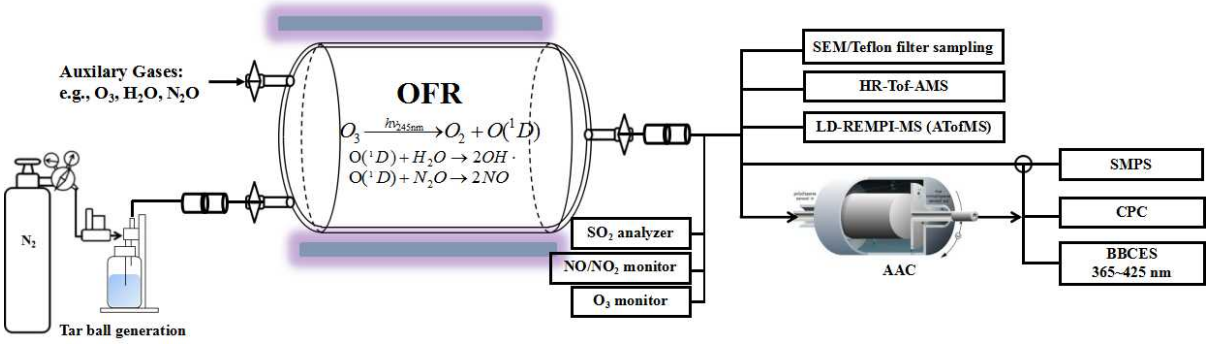

1119

1120 **Figure 1.** Experimental setup for laboratory generation and aging of tar ball aerosol: including generation setup, OFR

1121 photochemical aging, gaseous-particulate chemical monitoring, particle size distribution and optical properties measurements.

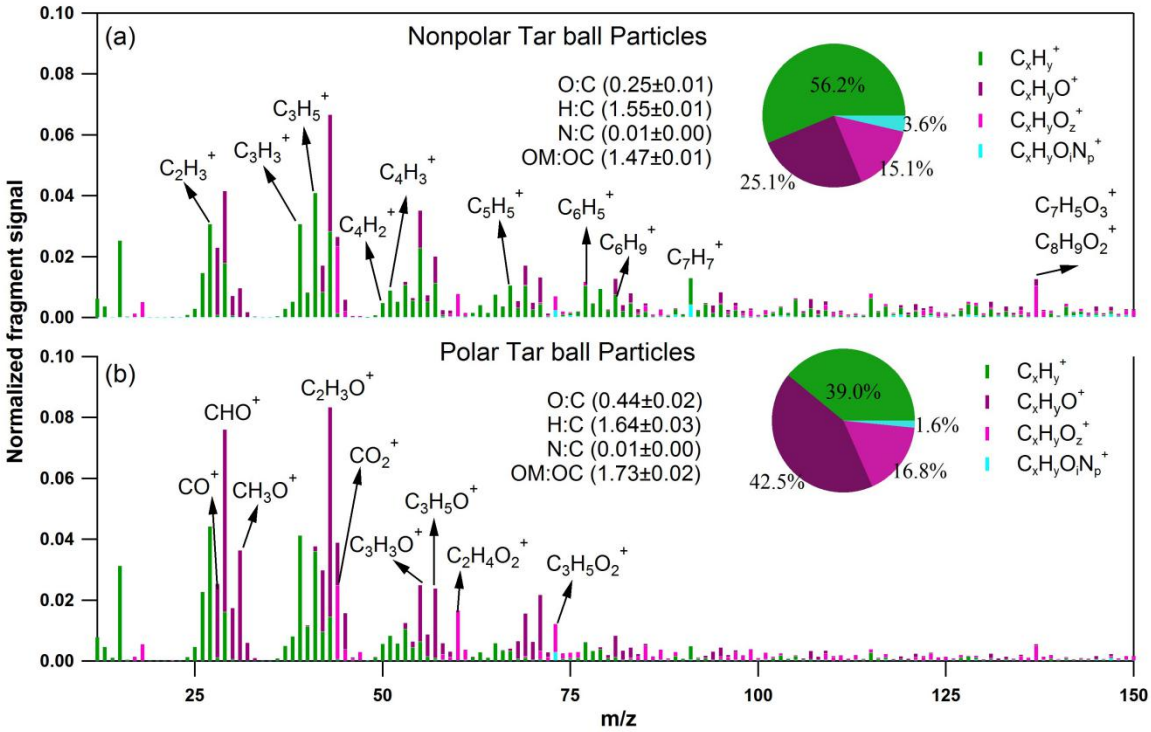

1122

1123 **Figure 2.** High-resolution AMS mass spectra of fresh polar and nonpolar tar ball particles. Four ion groups are grouped for

1124 clarity as: $C_xH_y^+$ (green), $C_xH_yO^+$ (purple), $C_xH_yO_z^+$ (z>1) (violet), $C_xH_yO_iN_p^+$(i≧0, p≧1) (light blue). The mass fractions of

1125 the four fragment groups are presented by pie-charts.

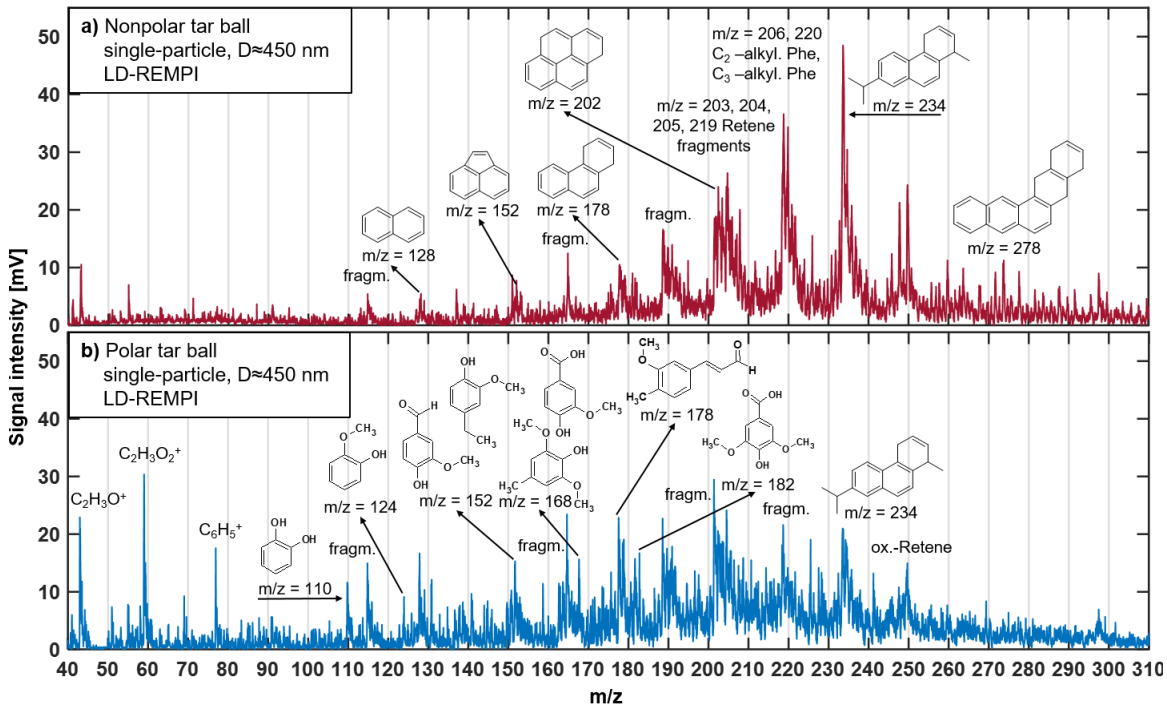

Figure 3. LD-REMPI mass spectra of exemplary single tar ball particles, some feature peaks were identified and labeled. a) Nonpolar tar ball spectra shows predominantly alkyl-substituted and unsubstituted PAHs. b) Polar tar ball spectra reveals many oxidized aromatics, e.g., methoxy-phenol, benzenediol. Note the softwood combustion marker retene at *m/z*=234, its characteristic fragments (*m/z*=203, 204, 205, 219) and possible retene derivatives (*m/z*=248, 250).

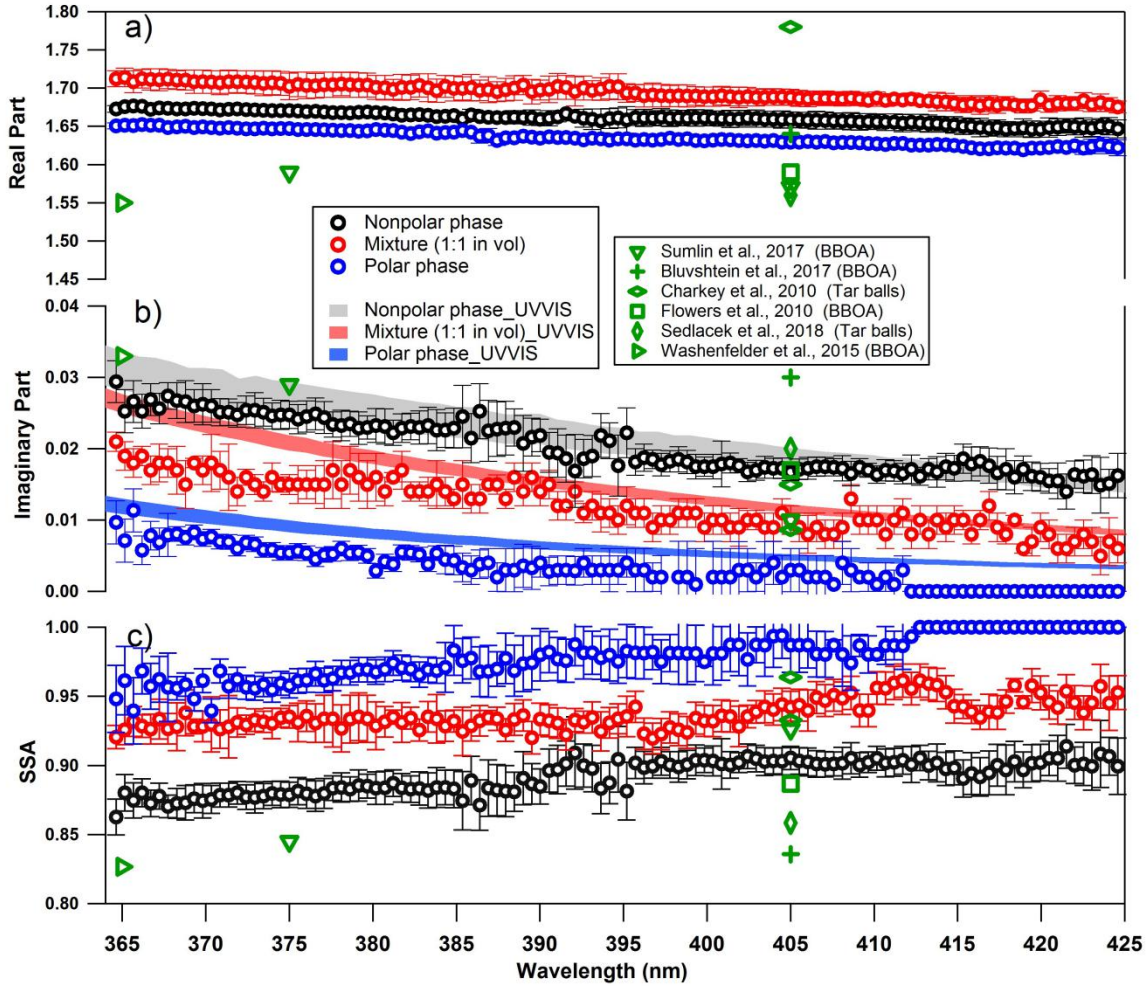

Figure 4. Wavelength-dependent RI and SSA for tar ball particles generated from polar, nonpolar and mixture of the two phases tarry solutions (only retrieval for mixture of 1:1 in vol. is shown for clarity, optical results for the rest two mixtures can be found in supporting materials). The shaded areas indicate the upper and lower limits of the imaginary part calculated from UV-VIS spectra of methanol extracts from the corresponding tar ball particles samples: a) real part, b) imaginary part, and c) SSA calculated for 150 nm particles. Overplayed in green symbol are previous measurements of biomass burning from the literature.

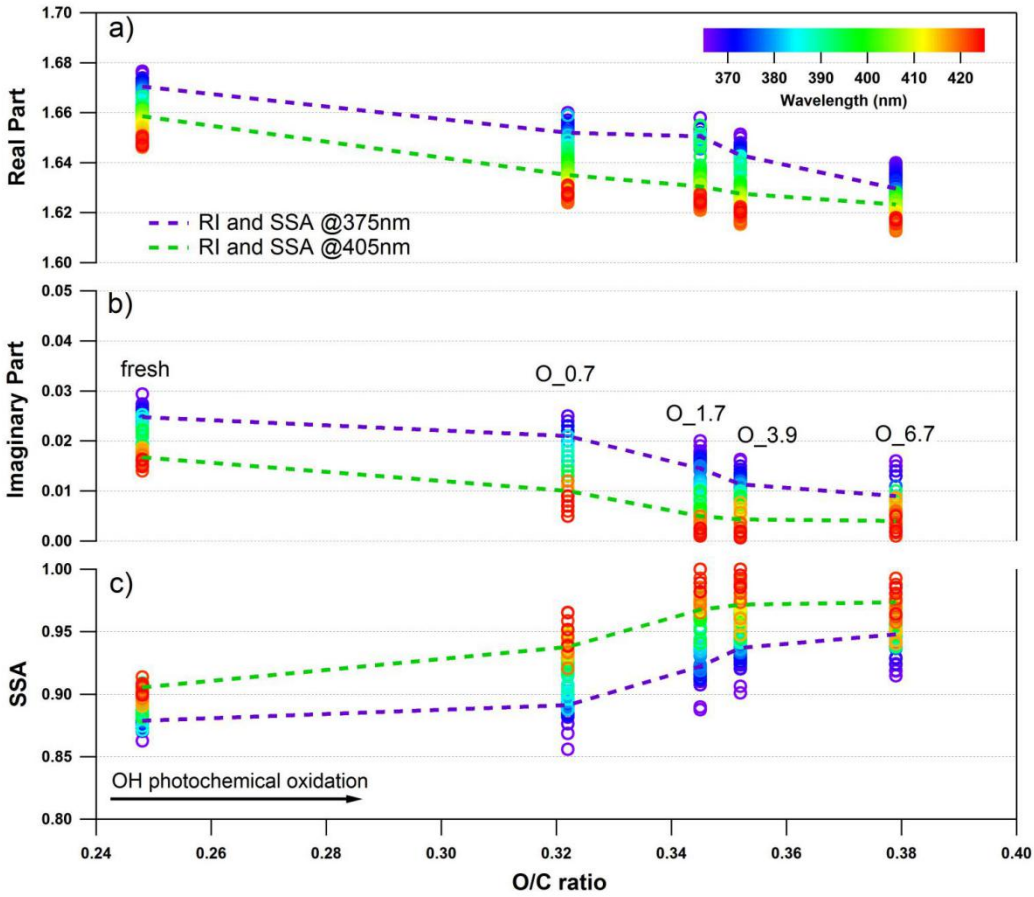

Figure 5. Evolution of the retrieved wavelength-dependent complex RI and SSA as a function of O:C ratio for tar ball particles upon OH photochemical oxidation: a) real part, b) imaginary part, and c) SSA calculated for 150 nm particles. The color scale shows the span in the RI for the wavelengths measured from 365 to 425 nm. For clarity, error bars for O:C ratio (±0.01), RI (±0.007 for real part, and ±0.003 for imaginary part on average), and SSA (±0.006) are not shown. Two dashed lines trace the RI and SSA at 375 nm (purple) and 405 nm (green). O_0.7~O_6.7 represent equivalent atmospheric photochemical oxidation for 0.7 and up to 6.7 days.

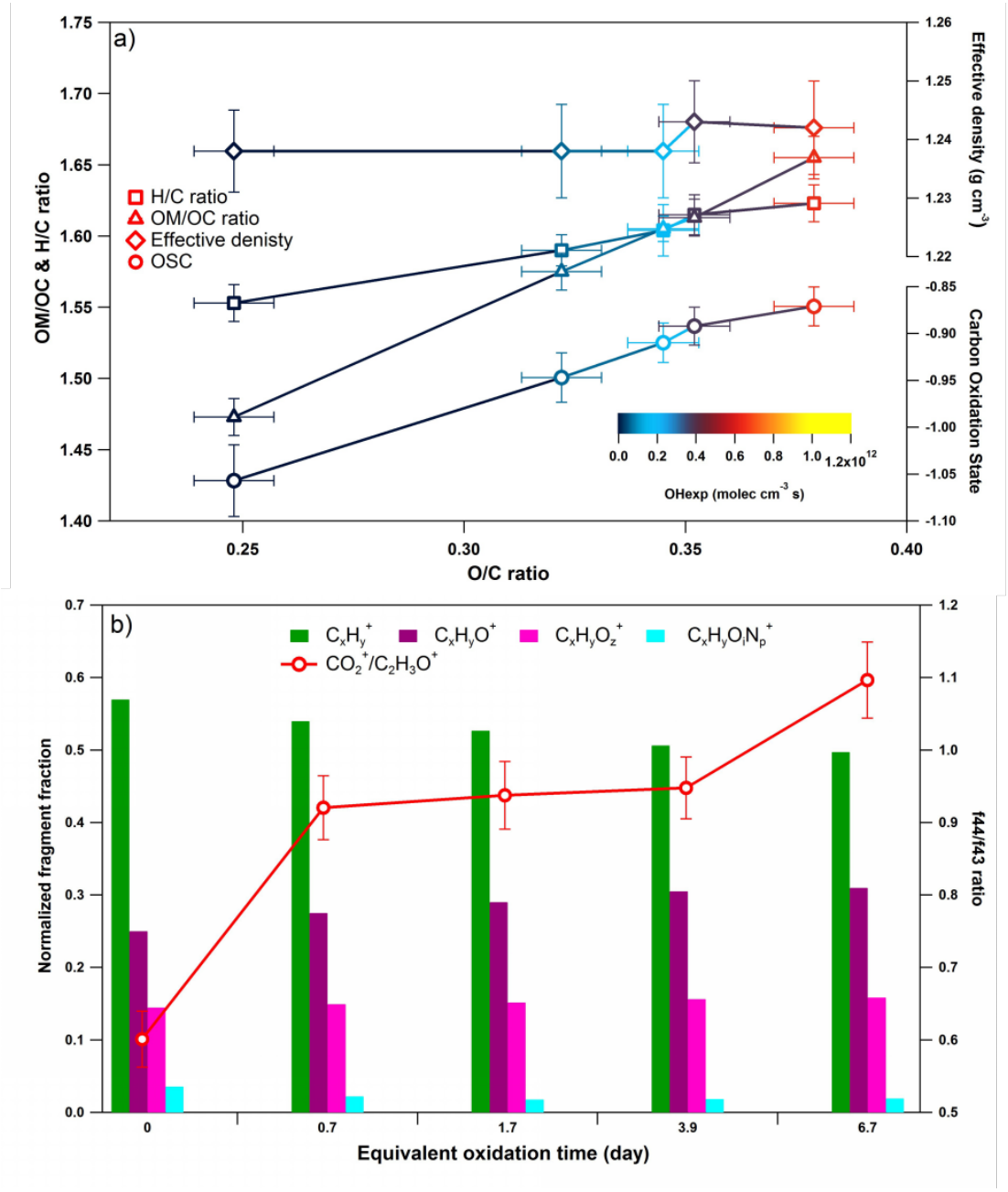

1144 **Figure 6.** Dynamic changes for the chemical characteristics of tar ball particle under NOx-free OH photochemical oxidation:

1145 a) OM/OC. H:C ratio, particle density, and average carbon oxidation state ($\overline{OSc}$) changes as a function of O:C ratio; b) mass

1146 spectra evolution with oxidation times in term of $C_xH_y^+$, $C_xH_yO^+$, $C_xH_yO_z^+$, and $C_xH_yO_iN_p^+$ fragment groups.

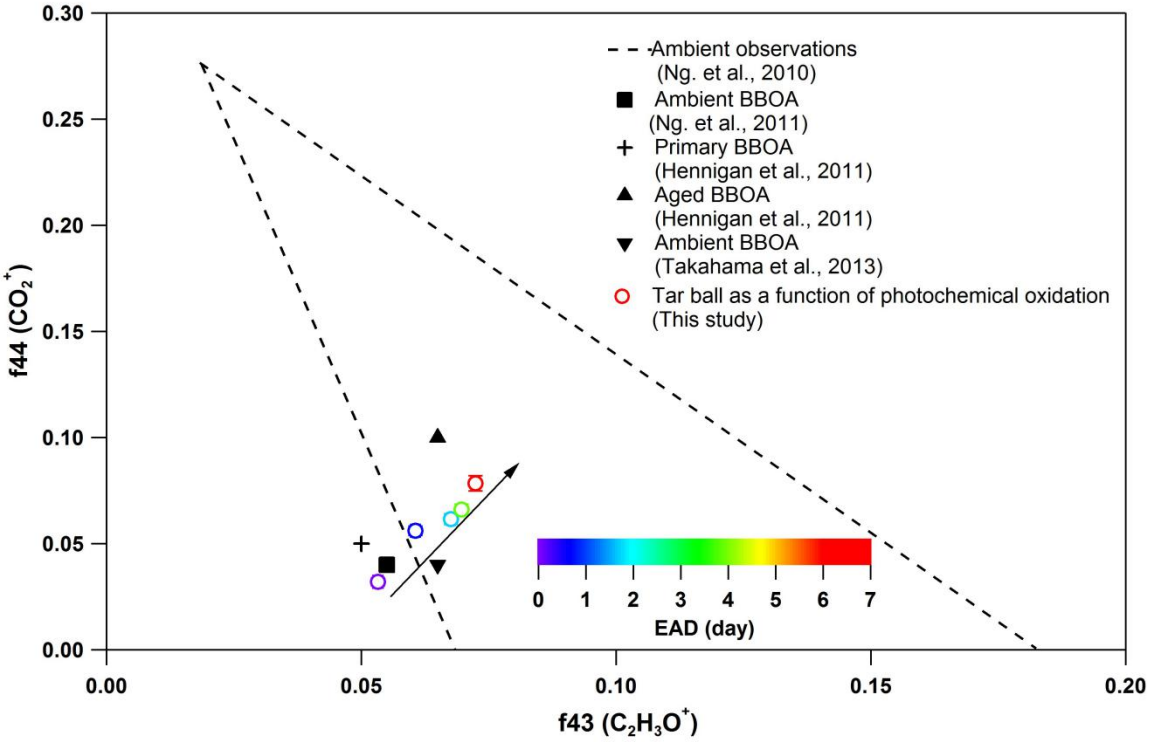

1147

1148 **Figure 7.** Comparison of f44 and f43 values from ambient data sets (Ng. et al., 2010) and values from ambient biomass burning

1149 organic aerosol. The hollow circles present tar ball result in this work, and color legend indicate equivalent atmospheric

1150 oxidation days, black arrow more clearly shows the extent of NOx-free photochemical oxidation in this study.

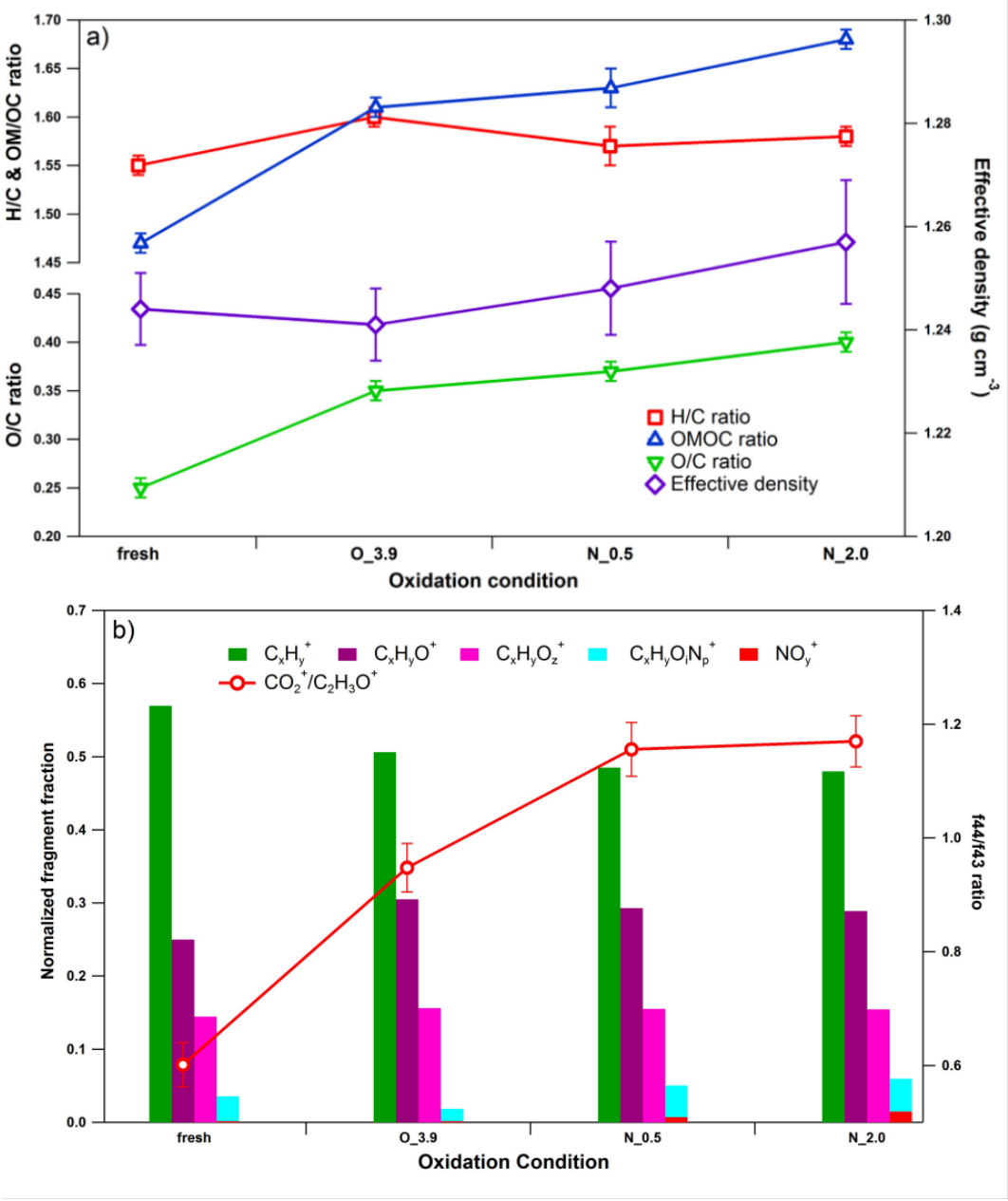

Figure 8. Dynamic changes for chemical characteristics of tar ball aerosols under NO_x-dependent OH photochemical oxidation: a) OM/OC, O:C, H:C, and particle density changes; b) mass spectra changes with different oxidation conditions in term of $C_xH_y^+$, $C_xH_yO^+$, $C_xH_yO_z^+$, and $C_xH_yO_zN_p^+$ fragment groups. $C_xH_yO_zN_p^+$ include all nitrogen-containing fragments, (e.g., $C_xH_yON^+$, $C_xH_yO_zN_i^+$, $C_xH_yN^+$, etc.), NO_y^+ include NO^+ and NO_2^+. O_3.9 represents 3.9 days equivalent atmospheric photochemical aging in absence of NOx, N_0.5 and N_2.0 indicate photochemical oxidation with 0.5 and 2.0 vol.% N_2O addition at ~4.0 days atmospheric oxidation.

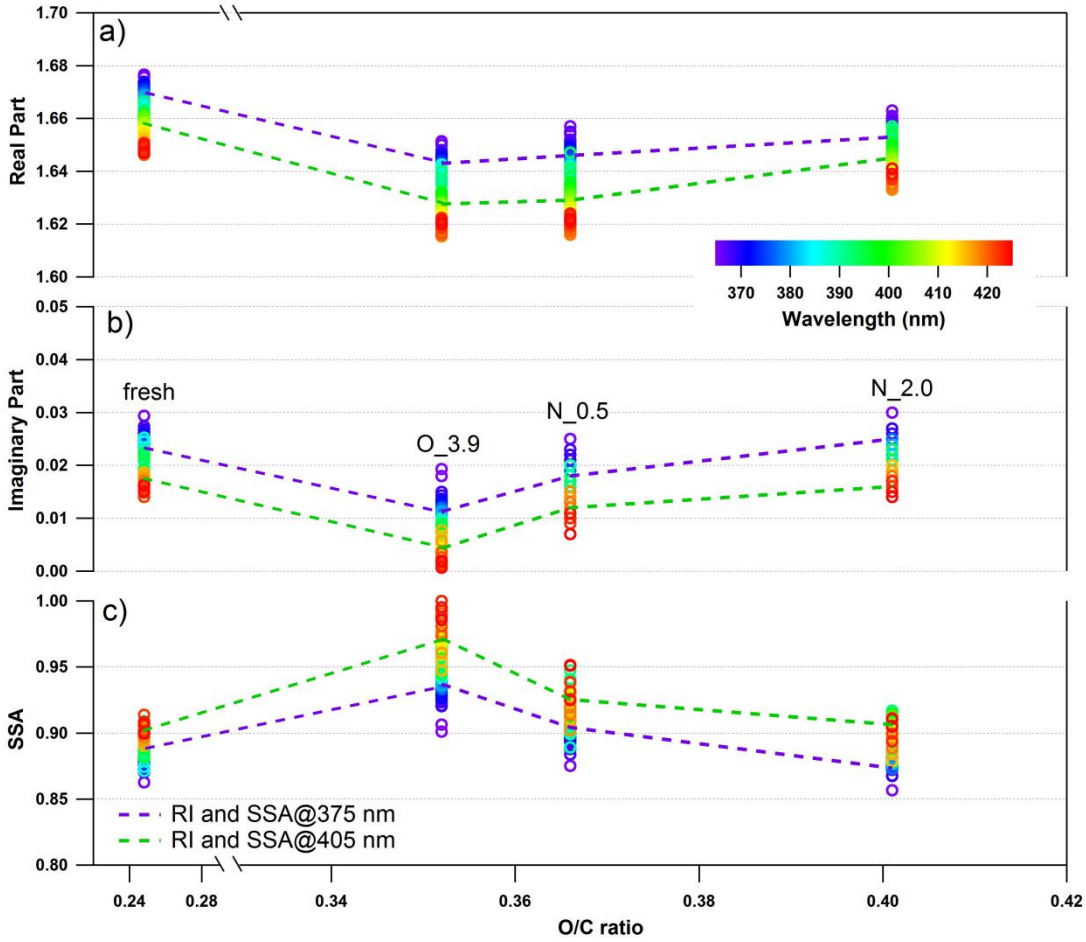

1157

1158 **Figure 9**. Changes of retrieved spectra-dependent RI as a function of O:C ratio for tar ball particles upon NOx-dependent

1159 photochemical oxidation: a) real part, b) imaginary part, and c) SSA calculated from 150 nm particles. For clarity, error bars

1160 for O:C ratio (±0.01), RI (±0.006 for real part, and ±0.003 for imaginary part on average), and SSA (±0.007) are not

1161 shown.O_3.9 represents 3.9 days equivalent atmospheric photochemical aging in absence of NOx, N_0.5 and N_2.0 indicate

1162 photochemical oxidation with 0.5 and 2.0 vol.% N2O addition at ~4.0 days atmospheric oxidation.

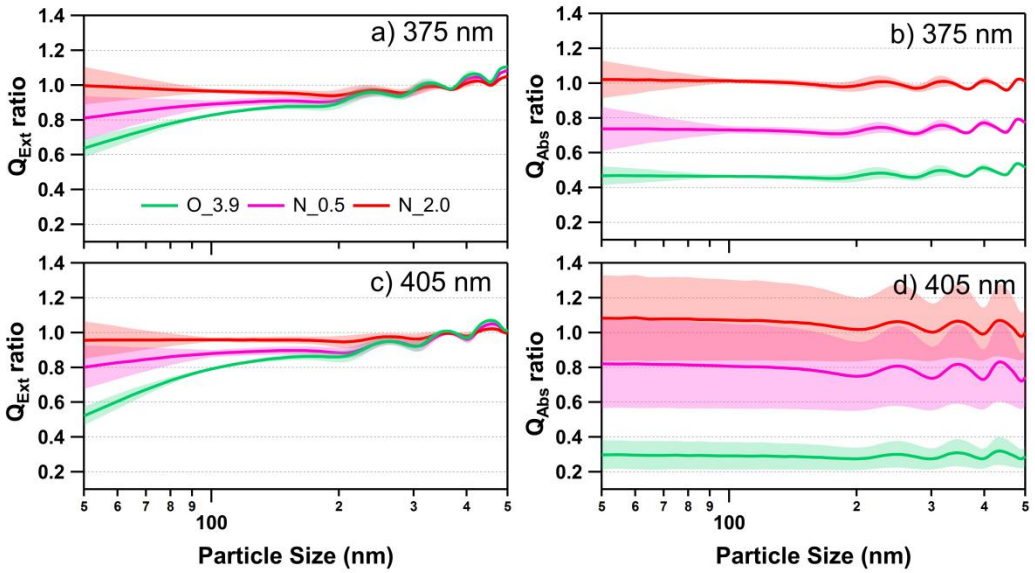

Figure 10. Size-resolved light extinction and absorption efficiency ratio of NO_x-dependent photooxidized tar balls compared to the fresh tar ball particles: a) and c) extinction ratios at 375 and 405 nm, b) and d) absorption ratios at 375 and 405 nm. O_3.9 represents 3.9 days equivalent atmospheric photochemical aging in absence of NOx, N_0.5 and N_2.0 indicate photochemical oxidation with 0.5 and 2.0 vol.% N_2O addition at ~4.0 days atmospheric oxidation.

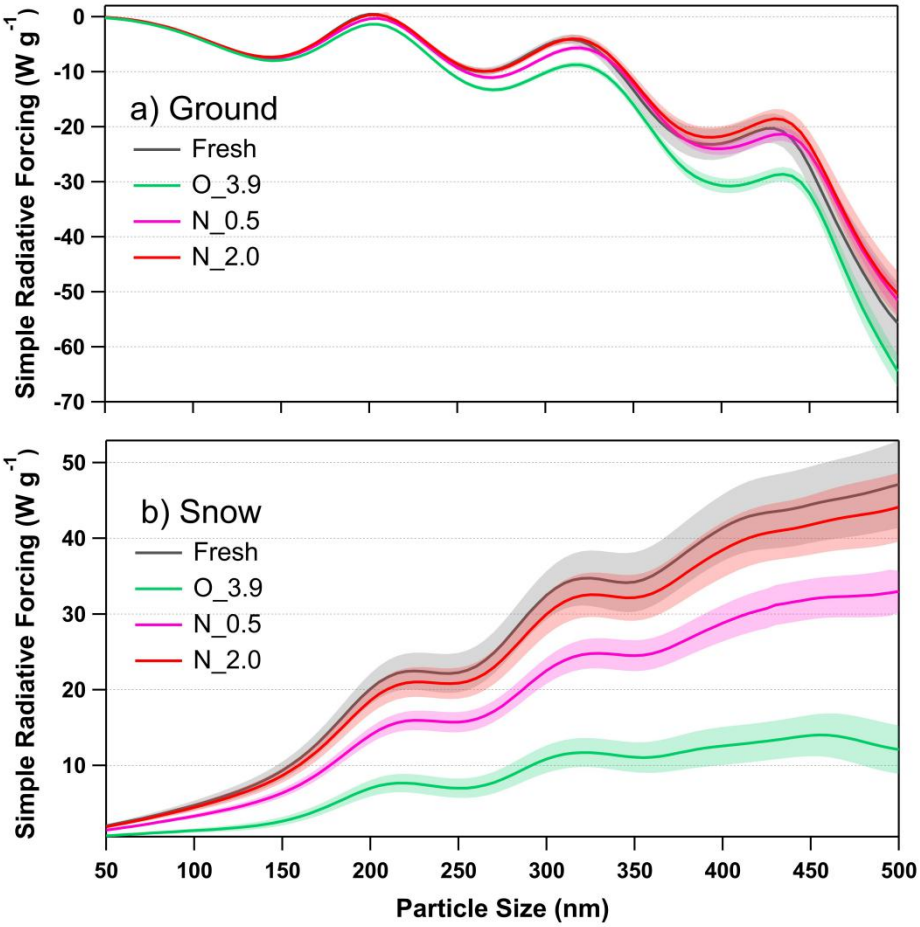

1168

1169 **Figure 11.** Calculated size-resolved simple radiative forcing (SRF, W g^{-1}) by tar ball aerosols, integrated over
1170 365~425 nm incident solar irradiation for fresh and NOx-dependent photooxidized tar balls: a) ground-based
1171 radiative forcing, b) snow-based radiative forcing.